

DeepISMNet: Three-Dimensional Implicit Structural Modeling with Convolutional Neural Network

Zhengfa Bi¹, Xinming Wu¹, Zhaoliang Li², Dekuan Chang³, and Xueshan Yong³

¹School of Earth and Space Sciences, University of Science and Technology of China, Hefei, Anhui, P.R.China.

²China Aero Geophysical Survey and Remote Sensing Center for Natural Resources, Beijing, P.R.China.

³Research Institute of Petroleum Exploration & Development-NorthWest(NWGI), PetroChina, Gansu, Lanzhou, P.R.China.

Correspondence: Xinming Wu (xinmwu@ustc.edu.cn)

Abstract. Implicit structural modeling using sparse and unevenly distributed data is essential for various scientific and societal purposes ranging from natural source exploration to geological hazard forecasts. Most advanced implicit approaches formulate structural modeling as least-squares minimization or spatial interpolation, using various mathematical methods to solve for a scalar field that optimally fits all the inputs under an assumption of smooth regularization. However, these approaches may not reasonably represent complex geometries and relationships of structures and may fail to fit a global structural trend when the known data are too sparse or unevenly distributed. Additionally, solving a large system of mathematical equations with iterative optimization solvers could be computationally expensive in 3-D. To deal with these issues, we propose an efficient deep learning method using a convolution neural network to create a full structural model from the sparse interpretations of stratigraphic interfaces and faults. The network is beneficial for the flexible incorporation of geological empirical knowledge when trained by numerous synthetic models with realistic structures that are automatically generated from a data simulation workflow. It also presents an impressive characteristic of integrating various types of geological constraints by optimally minimizing a hybrid loss function in training, opening new opportunities for further improving the structural modeling performance. Moreover, the deep neural network, after training, is highly efficient to generate structural models in many geological applications. The capacity of our approach for modeling complexly deformed structures is demonstrated by using both synthetic and field datasets, in which the produced models can be geologically reasonable and structurally consistent with the inputs.

1 Introduction

A geological model structurally consistent with the subsurface is essential for well understand the subsurface spatial organization and quantitatively simulating geological processes for a wide variety of earth science applications (Li et al., 2016; Wellmann and Caumon, 2018). Structural modeling is aimed to accurately represent the geometry of geological structures with a numerical model by using various mathematical methods. The traditional modeling approach can be described as explicit or surface modeling (Caumon et al., 2009). It reproduces the complex geometries and relationships of structures by digitizing the interpreted surface elements and their arrangements, and the resultant model typically incorporates a series of geological interfaces derived by a triangulation algorithm. In addition to being time-consuming, the modeling process is also related to each individual geologist's interpretation and might not be replicated by others (Caumon et al., 2009; Chaodong et al., 2010).

25 Recently, more and more implicit structural modeling methods have been proposed for constructing geological models because of their efficient, updatable, and reproducible characteristics (Calcagno et al., 2008; Caumon et al., 2012; Hillier et al., 2014; Laurent et al., 2014; Collon et al., 2015). The implicit method is distinguished from the explicit approach because it consists in interpolating field structural observations into a volumetric scalar function that is defined on the entire region of interest to implicitly represent geological structures. In this function, the geological interfaces are embedded as its iso-
30 surfaces, while the structural discontinuities are indicated by discontinuous value jumps of the function. Thus, the scalar function is also called the implicit model. The implicit method benefits from incorporating all available geological information into the resultant model by integrating the observed data and the empirical knowledge, providing an effective alternative to reproduce the geometry of the subsurface from a global view (Calcagno et al., 2008; Fossen, 2016). The input structural data of the implicit method typically included various types of modeling objects, such as spatial points, vectors, polylines, and
35 surfaces, interpreted from field observations. The empirical knowledge can be manually inferred from the structural data by the geologists and geophysicists to define the possible geometrical relationships among the geological interfaces and drive the modeling behaviors of the implicit methods. The output model requires representing geologically reasonable structures while honoring the input structural data. As it is hardly possible to observe the ground truth of subsurface, the geological structures are often heterogeneously sampled in a limited number of highly developed mining and oil fields. This arises the necessity of
40 adding prior geological rules and assumptions to constrain the modeling process. For example, the existing implicit interpolants typically impose explicit smoothness criteria to simplify local variations for computing a unique structural model.

The discrete smooth interpolation (DSI) is one class of implicit methods that compute structural models by discretizing the scalar function on a volumetric mesh (Mallet, 1988, 1992, 1997, 2014; Souche et al., 2014; Renaudeau et al., 2019). In DSI and its variant approaches, structural modeling is performed by solving a least-squares minimization problem with smooth
45 constraints to compute a scalar field compatible with the inputs. This smooth constraint incorporates empirical geological knowledge into the modeling process with a fundamental assumption that the desired model should be as smooth as possible. However, the mesh elements prohibit from crossing structural discontinuities because the scalar function is always continuous on the mesh elements, and the method cannot correctly estimate the gradients of the scalar function near the faults or unconformities (Shewchuk, 2002). To deal with this problem, we require to compute a constrained unstructured mesh by in-
50 dependently modeling the discontinuous structures, such that the approaches can work well in these cases. In addition to DSI, the potential field method (PFM) is another class of implicit approaches (Lajaunie et al., 1997; Jessell, 2001; McInerney et al., 2007; Phillips et al., 2007). PFM typically formulates structural modeling as a dual cokriging interpolation (Chiles et al., 2004; Calcagno et al., 2008) or as a radial basis function interpolation (Carr et al., 2001). In comparison to DSI, although the models are evaluated on a volumetric mesh for a visual purpose, PFM does not use any mesh grids when computing the scalar function.
55 Instead, structure interpolation is fully dependent on the distribution of the observed structural data and the influence range of each data point is determined by the chosen interpolants. However, PFM usually yields a dense system to scale the influence of the interpolants over the entire volume for obtaining a structurally valid solution, which causes the computational cost quickly increase with the input data size and soon become prohibitive.

The existing approaches exhibit many promising characteristics, however, reproducing structures of highly deformed regions remains a challenging task regarding geological consistency because the modeling reliability depends on the availability and quality of the observed data. Structural interpolation fully guided by mathematical equations might not always produce a geologically valid model given sparse or unevenly distributed data (sparse or clustered) in some complex geological circumstances. Corresponding structural models often have erroneous geometries that are inconsistent with geological knowledge and spatial relationships with relevant structures. This problem is mainly attributed to the limited constraints that are permitted in structural interpolants, in which all the data and knowledge are mathematically represented as a form of linear constraints to compute a continuous scalar function as smoothly as possible. Although this assumption is helpful to derive a unique model, imposing such a smoothness criterion might compromise the influence of local structural variations and negatively impact the modeling accuracy of highly variant structures (de Kemp et al., 2017; Hillier et al., 2021). Because the modeling flexibility is limited to the models that a specific interpolant can generate, the implicit methods usually suffer from artefacts or geometrical features physically impossible from a geological modeling point of view. Therefore, it is significant to improve implicit modeling by flexibly aggregating all available geological information to ensure that we can obtain a structurally reasonable model (Grose et al., 2018, 2021).

In this study, we present a deep learning method using a convolutional neural network (CNN) as an alternative to conventional implicit structural modeling. Deep learning is a type of data-driven and statistical approach that estimate an implicit function that maps inputs to outputs from past experiences or example data by minimizing given quality criteria (Donmez, 2010). In contrast with traditional approaches, deep learning is beneficial for making a prediction without solving a linear system of equations under prior mathematical constraints at cost of expensive computation. Among current learning-based methods, CNN is essential for its remarkable power in analyzing geometrical features and capturing complexly nonlinear spatial relations given a sufficiently large training dataset. To find an optimal trade-off between accuracy and efficiency, there exist many convolutional modules available for constructing the CNN architecture, such as depth-wise separable convolution (Chollet, 2017; Howard et al., 2017), attention mechanism (Iandola et al., 2016; Howard et al., 2019), and residual learning structure (Sandler et al., 2018). It is not a surprise that the CNN-related applications in geosciences have been growing rapidly during the past years, including seismic interpretation (Shi et al., 2019; Wu et al., 2019; Geng et al., 2020; Bi et al., 2021), earthquake detection and location (Wu et al., 2018; Perol et al., 2018), remote-sensing image classification (Chen et al., 2016; Maggiori et al., 2016), geochemical map interpolation (Kirkwood et al., 2022), and so on. It is worth noting that a novel learning-based method using Graph Neural Networks (GNN) (Hillier et al., 2021) has been recently developed to integrate structural observations into a graphic mesh encoding all relevant geometrical relations for producing a structural scalar field. This method presents a promising foundation for introducing interpolation constraints that current implicit mathematical methods cannot permit by comparing the prediction and the structural observations, showing an impressive performance to deal with implicit and discrete geological data. However, the method cannot exactly reproduce the modeling results under the same inputs as the network parameters are initialized randomly in each run of computation. By measuring structural errors only on the scalar field constraints, it may fail to incorporate information associated with structural discontinuities into graphic structures, such as representing the spatial relation of the modeling elements across faults. Another potential limitation results from a bottle-

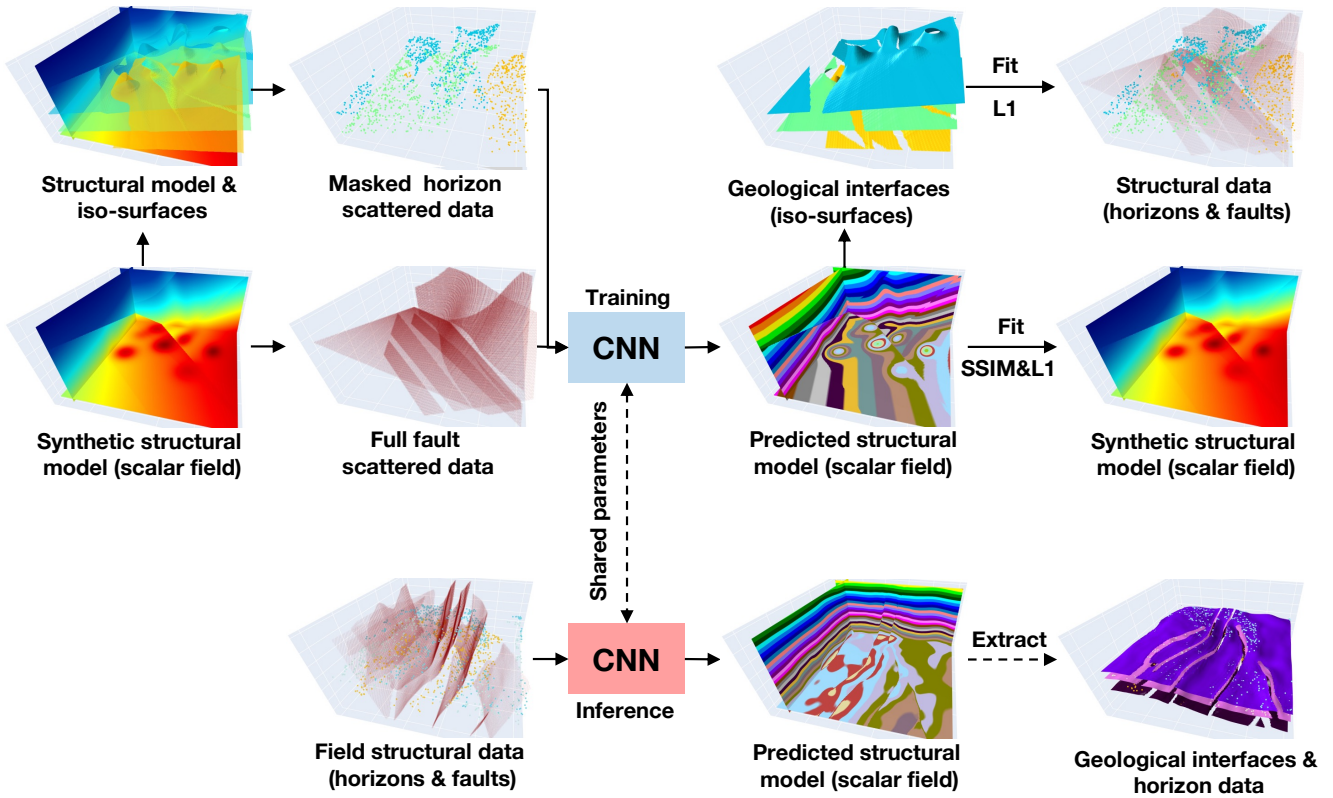


Figure 1. Our implicit modeling method produces a volumetric scalar function as an implicit representation of all the geological structures from input point data by using CNN. Trained with numerous synthetic data, the network can be applied to field structural data to efficiently predict a geologically reasonable model that well matches the input structure data.

necking problem in the current GNN's architecture (Alon and Yahav, 2020), in which further improvement of the modeling capacity is restrained by network depth with a few layers. A network with a simple structure might not be sufficient to deal with relatively complex geological structures.

As is shown in Figure 1, we formulate implicit modeling as an image inpainting problem with deep learning, in which a full structural model is estimated from the sparse and heterogeneously sampled data based on the past experiences and knowledge learned from the training dataset. This characteristic permits a flexible introduction of empirical geometrical relations and structural interpolation constraints by defining an appropriate loss function to measure the differences between the structural models being compared. Our network, also called DeepISMNet, can produce a scalar field as an implicit representation of all the structures from various types of structural data including horizons that encode the stratigraphic sequence of the sampled interfaces and faults that indicate geological boundaries. We parameterize faulting and folding simulations to automatically create numerous geological models with realistic and diverse structures by randomly choosing parameters within reasonable ranges, which are considered as the example data or labels. In training the network, we randomly extract horizon and fault

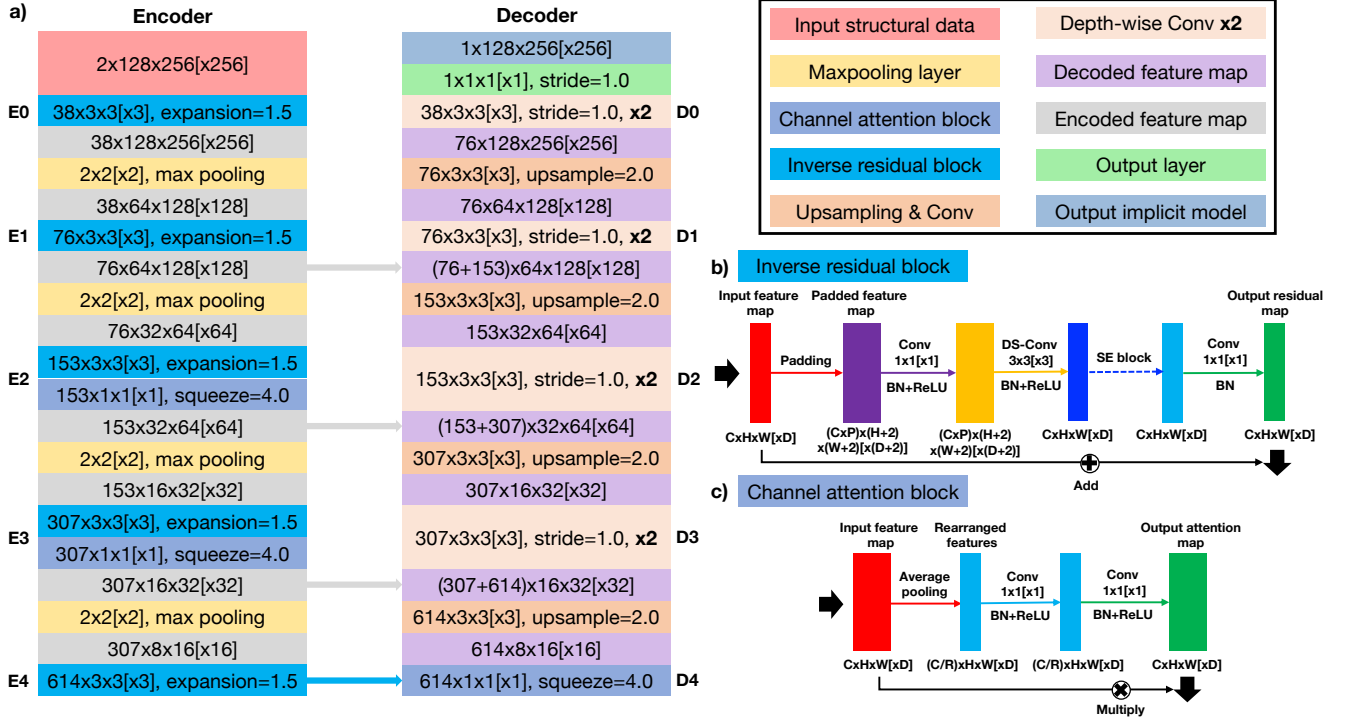


Figure 2. Our network has a U-shaped architecture that consists of encoder and decoder branches shown in (a). The encoder uses an inverse residual block (b) supplemented by a lightweight channel-based attention (c) to deal with the input structural data at each of the 5 different spatial scales. The decoder computes the hidden representations at the corresponding 5 resolution scales to form a sufficiently deep CNN. Note that square brackets represent the dimensional expansion of the corresponding 2-D networks to 3-D ones.

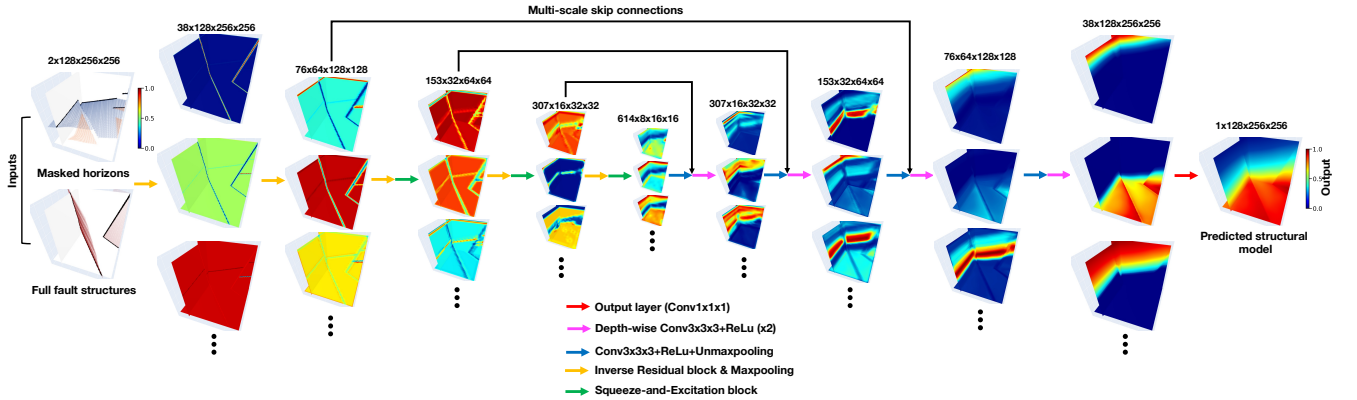


Figure 3. The normalized hidden feature representations computed in each spatial scale of the 3-D structural modeling networks.

structures from these models to further generate unevenly distributed structural data as inputs which the network takes to predict a full geological model as output. Also, we demonstrate that the normal vectors sampled near geological interfaces can be used to constrain local structural orientations associated with the gradients of the predicted model. In training the CNN, we define a hybrid loss function that combines element-wisely measurement on the input horizon data and multi-scale structural similarity over the local sliding windows to guarantee a geologically consistent prediction. Once obtaining an implicit structural model, we can simply compute the horizon surfaces by using the iso-surface extraction method while detecting the faults near the local value jumps or discontinuities (Figure 1). We find that the trained CNN can efficiently create a geologically reasonable and structurally consistent model in both synthetic and field data applications, showing promising potential for further leveraging deep learning to improve modeling capacity in many geological applications. In addition, the solutions are reproducible as it is not necessary to randomly initialize the parameters of the trained network at each modeling process.

We organize this paper as follows. In the Methodology section, we describe the CNN architecture designed for implicit modeling and its associated loss function definition. In the Data Preparation section, we introduce the methodology used to automatically generates training data and simulate the partially missing horizons. The Implementation and Application sections include both synthetic and real-world case studies to verify the performance of our network in representing complex geological structures. The Discussion section presents the promising characteristics of the proposed CNN approach and its current limitations and possible improvements that we will focus on in future research. Finally, we summarize our work in the Conclusions section.

2 METHODOLOGY

In this section, we describe the CNN architecture and its associated loss function used in training the network to generate implicit structural models.

2.1 Network Architecture

Our developed CNN architecture uses a U-shaped framework modified from UNet and its associated variants (Ronneberger et al., 2015; Zhou et al., 2018), where we include further improvements based on previous works to find an optimal trade-off between accuracy and efficiency in geological modeling. In many image recognition tasks where inputs and outputs share the same spatial resolution, UNet is typically regarded as a standard principle due to its excellent performance (Lin et al., 2017; Yu et al., 2018a). Its great representational power results from a linked encoder-decoder architecture, in which features are first downsampled at multiple spatial resolutions in the encoder and then recombined with their upsampled counterparts through skip connections in the decoder. The localized components of the inputs are typically extracted at an early stage of the CNN, while the relatively high-level and global features are obtained when the receptive fields are increasingly large in deep convolutional layers. Thus, as the hidden representations with different spatial resolutions have much distinctive geometrical information, systematically aggregating the hierarchical multi-scale features with skip connections is attributed to a reliable and stable structural field prediction. Furthermore, the low-level features computed from the shallow layers better follow the

input structures than the deep high-level features because the structural information might be gradually missing in recursive feature compressions at the downsampled spatial resolutions. The use of skip connections also helps to enhance the low-level features and produce a model structurally consistent with the inputs.

We show the proposed 2-D and 3-D CNNs with the same architecture in Figure 2a, in which square brackets represent the dimensional expansion of the corresponding 2-D networks to 3-D ones. The encoder branch in our proposed network consists of 5 successive inverse residual blocks dealing with the input structural data at 5 different spatial scales (from **E0** to **E4**) related to 2, 4, 8, 16, and 32 downsampling rates, respectively. When downsampling the hidden representations at each spatial scale by using the max pool layer, the encoder simultaneously expands its channels. As is shown in Figure 2b, we adopt a linear bottleneck and inverted residual architecture in each block to make an efficient convolutional structure by leveraging the low-rank nature of the inputs. This structure is composed of a $1 \times 1[\times 1]$ expansion convolutional layer, a $3 \times 3[\times 3]$ depth-wise convolutional layer, and another $1 \times 1[\times 1]$ projection convolutional layer, and each convolution is followed by a Batch Normalization (BN) and a Rectified Linear Unit (ReLU). The two $1 \times 1[\times 1]$ convolutional layers at the ends of the depth-wise convolutional layer are designed to expand the inputs to higher-dimensional feature space (one and a half times of the channels) and project them back to the output channels, such that the inverse residual block forms a compact feature embedding to improve the expressiveness of the nonlinear transformation at each channel. We did not try a larger expansion factor because of the GPU memory limitation, but we would suggest choosing a larger size if the GPU memory is allowed. With a residual connection over the expansion and projection convolutional layers, the block is formulated as a residual learning function to speed up the backpropagation of gradient responses. Although the encoder layers aggregate abundant information through recursive channel expansions, not all the features are useful for modeling geological structures. There exist many structurally irrelevant features with mostly zeros across channels due to the sparse and heterogeneous characteristics of the inputs. Treating all channel-wise features equally would waste unnecessary computations to focus on the informative features and thus negatively influences the representational power of the network. To enhance the CNN's discriminative learning ability, we insert a lightweight channel-based attention module into the bottleneck structure of the inverse residual block in the last three spatial scales of the encoder. The attention block (Figure 2c) consists of squeeze and citation modules, in which the input features are first compressed into lower-dimensional feature space in the squeeze module and then transformed to the channel-wise attention weights with the same channels as the inputs in the citation module. This module (Hu et al., 2018) encourages the network to adaptively learn the relations across hundreds of high-level features with relatively global structural information and rescale their importance to stabilize the modeling process by emphasizing the informative features and suppressing the irrelevant ones.

The decoder branch includes the 5 spatial scales (from **D4** to **D0**) consistent with the encoder to form a sufficiently deep network and large receptive field for structural interpolating. It is responsible for integrating the hidden representations from the previous unmaxpooling layers and the encoder skip connections while compensating for the spatial resolution mismatch between the concatenated features. In each spatial scale, the upsampled decoded features are first concatenated with their downsampled counterparts in the encoder branch and then sequentially fed into the two convolutional layers to further refine the features. We use depth-wise separable convolutional layers (Howard et al., 2017) as an efficient replacement for the traditional

convolutional layers. The depth-wise separable convolutional layer factorizes the convolutional operation as two separate layers including a lightweight $3 \times 3 \times 3$ convolutional layer for filtering features within each channel and a relatively heavy $1 \times 1 \times 1$ convolutional layer for combining features across channels. By splitting the standard convolution as the two-step process, we can dramatically reduce the computation complexity and the GPU memory to construct a lightweight decoder network. In the final layer, we adopt a simple linear transform implemented by a $1 \times 1 \times 1$ convolutional layer to cross all the decoded features for producing a full geological model.

Figure 3 visualizes the normalized hidden representations at each resolution scale of our 3-D structural modeling network that the inputs are passed through. As the amplitude ranges of the hidden representations are much varying from each other, we rescale them to obtain the normalized features with values restrained from zero and one for a visual purpose. Our CNN is designed to progressively complete structural features layer by layer through sequential non-linear convolutional units that are conditioned on the previous convolutions. As is displayed in Figure 3, the valid convolutional responses only exist near the input structures in the starting layer of the network. To spread geological structures elsewhere, every convolutional layer collects features from the previous layer outputs within an increasingly expanding receptive region by staking convolutions and recursively downsampling the input hidden features. Therefore, at the bottom layers of the network, the structural information in the inputs can be used to constrain the modeling process over the entire model from a global receptive region of view. This characteristic allows the network to correctly understand the relations of the spatially distant but contextually close features. Although weighting on spatial proximity is typically used in many traditional structural interpolation methods, the nearby features are not necessarily more significant than distinct ones for making geological-related predictions. For example, when the stratigraphic layers are located the opposite of a large shear zone or other discontinuous structures, the correlations of distinct data points computed from a global review can be helpful to capture a more accurate structural pattern.

2.1.1 Loss Function

The network provides an attractive characteristic to integrate various structural constraints by minimizing the corresponding errors between the predicted and reference models. For geologically valid CNN predictions, we combine element-wise accuracy with multi-scale structural similarity to define a hybrid loss function. We introduce notations and formal definitions used in this loss function. Let \mathbf{x} be reference structural model, and \mathbf{m} be its binary mask where the pixels or voxels on the input horizons are set to 1 and the rests are set to 0. The dimensional sizes of \mathbf{x} and \mathbf{m} are consistent with the samples in our training dataset. For each reference model \mathbf{x} , the CNN f_θ with trainable parameters θ takes horizon $\mathbf{h} = \mathbf{x} \odot \mathbf{m}$ and fault data \mathbf{f} and creates a structural field $\hat{\mathbf{y}} = f_\theta(\mathbf{h}, \mathbf{f})$ as outputs. We denote the predicted model replaced with the inputs on the points of the horizon data as $\mathbf{y} = \hat{\mathbf{y}} \odot (1 - \mathbf{m}) + \mathbf{x} \odot \mathbf{m}$.

In many geologically related regression problems, Mean Square Error (MSE) and Mean Absolute Error (MAE) are commonly used to element-wisely measure the accuracy of the solutions (Geng et al., 2020; Hillier et al., 2021). However, MSE typically emphasizes the elements with larger errors but is more tolerant of smaller ones, regardless of the underlying spatial pattern of the data. In comparison to MSE, MAE can be more sensitive to the local structural variations and reduce the artefacts

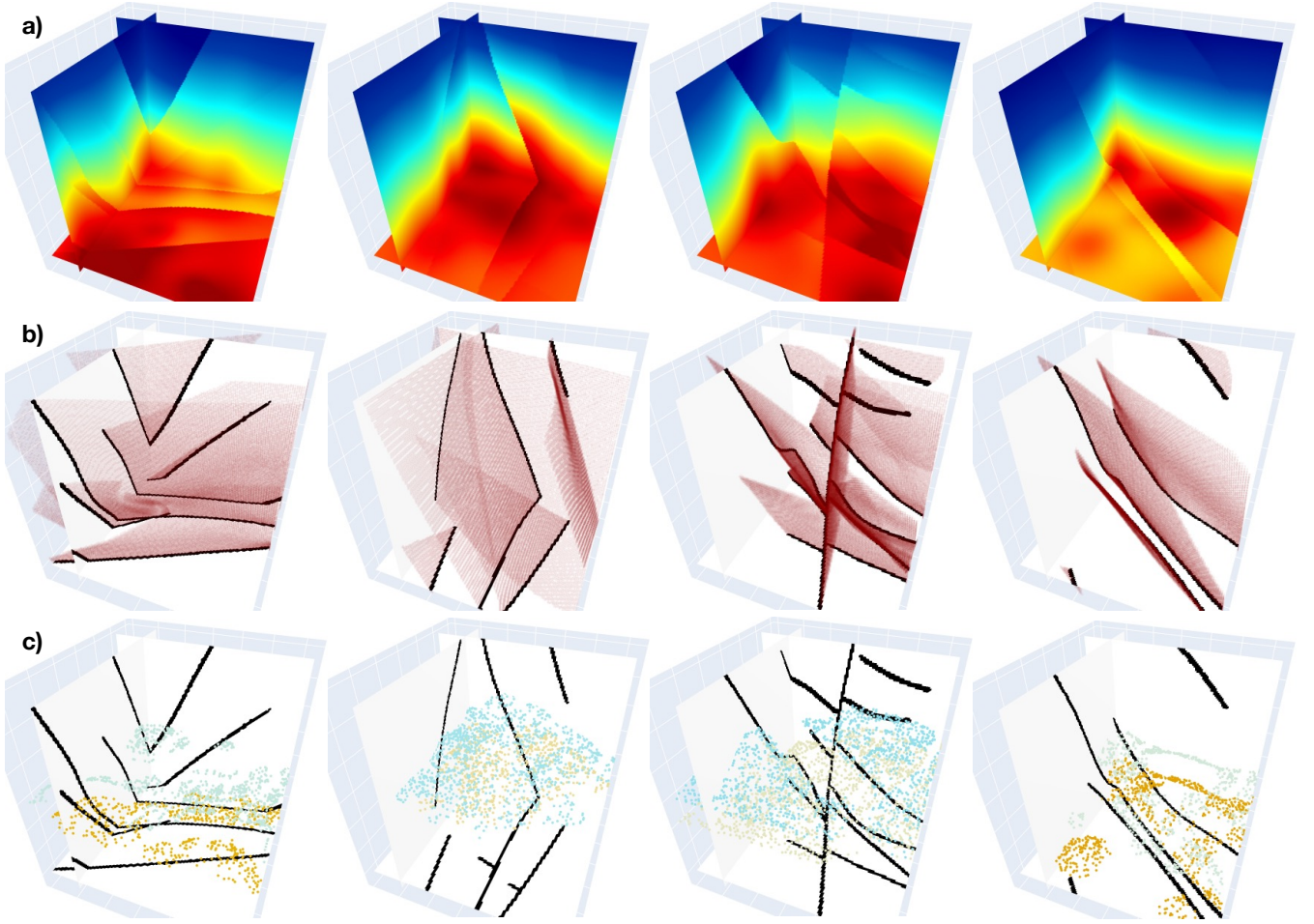


Figure 4. Four pairs of 3-D training data samples. The first row shows 3-D synthetic implicit structural models used as labels in training our 3-D network. The second and third rows, respectively, display the fault volumes and sparse horizon points extracted from the label models (first row), which are together used as inputs of the CNN.

caused by excessively penalizing large errors between modeling results and targets. We adopt masked MAE as a point-wise measurement in the hybrid loss function, which is formulated as follows:

$$\mathcal{L}_{\text{mae}}(\mathbf{p}) = \frac{1}{N} \sum_{p \in \mathbf{p}} |\mathbf{x}(p) - \hat{\mathbf{y}}(p)|, \quad (1)$$

where N represents the total number of the points within a square patch \mathbf{p} . We crop the patches from the same spatial location in the two structural models being compared.

Although MAE can outperform MSE in geological modeling scenarios, the results are still not optimal. CNN trained by using MAE alone might not correctly capture geometrical features that are represented by the distribution of the neighboring points,

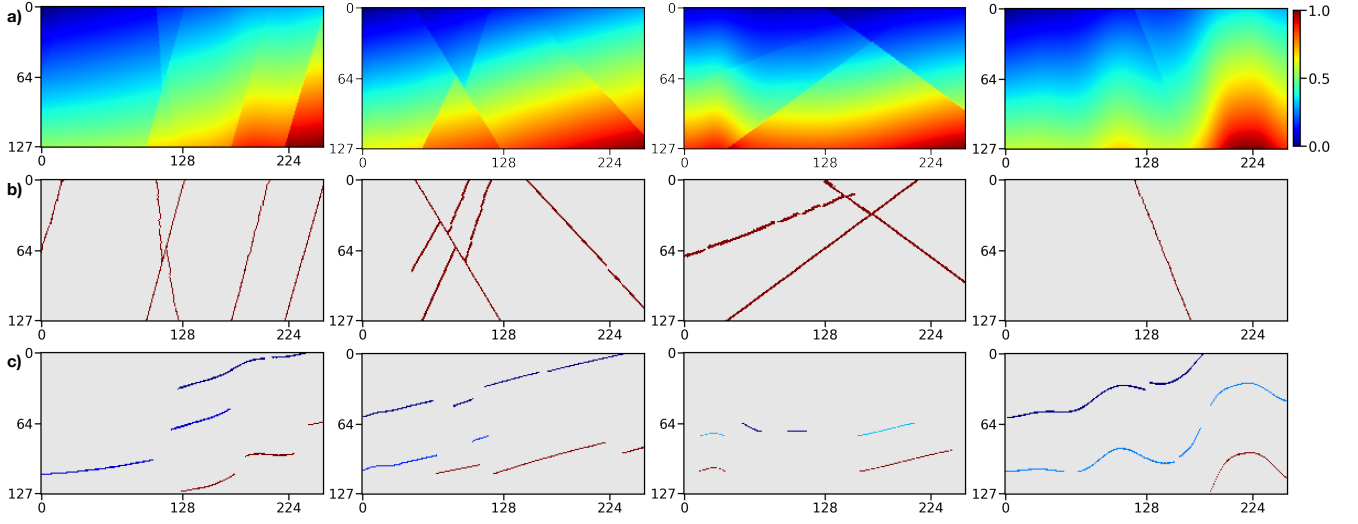


Figure 5. Four pairs of 2-D training data samples. The first row displays 2-D synthetic implicit structural models used as labels in training our 2-D CNN. The second and third rows, respectively, show the fault images and sparse horizon points extracted from the label models (first row), which are together used as inputs if the CNN. It is worth noting that the points denoted by the same color in each image of the third row correspond to the same horizon.

whereas blurring high-frequency and sharp structural discontinuities. Thus, the two models with similar MAE might appear significantly distinct structures, which negatively impacts the optimization of the CNN’s parameters. To alleviate such smooth effectiveness, we use a hybrid loss function by combining MAE with Structural Similarity (SSIM) (Wang et al., 2003, 2004; Zhao et al., 2016). By adaptively assigning higher weights to the structural boundaries in which the geological structures present significant contrasts, SSIM can better preserve the high-frequency geometrical features than the other loss functions. SSIM loss measuring the CNN prediction and the reference model within the patch \mathbf{p} can be represented as follows,

$$\begin{aligned}\mathcal{L}_{\text{ssim}}(\mathbf{p}) &= 1 - \left(\frac{2\mu_{\mathbf{x}}\mu_{\mathbf{y}} + C_1}{\mu_{\mathbf{x}}^2 + \mu_{\mathbf{y}}^2 + C_1} \right)^\beta \left(\frac{2\sigma_{\mathbf{xy}} + C_2}{\sigma_{\mathbf{x}}^2 + \sigma_{\mathbf{y}}^2 + C_2} \right)^\gamma \\ &= 1 - l(\mathbf{p})^\beta \cdot cs(\mathbf{p})^\gamma,\end{aligned}\tag{2}$$

where $\mu_{\mathbf{x}}$ and $\mu_{\mathbf{y}}$ represent the means of model \mathbf{x} and \mathbf{y} within \mathbf{p} , respectively. $\sigma_{\mathbf{x}}$ and $\sigma_{\mathbf{y}}$ are the variances, while $\sigma_{\mathbf{xy}}$ is the covariance of the two patches being measured. The means, variances, and covariance are computed by using an isotropic Gaussian filter G_{σ_g} with standard deviation σ_g and zero mean. Approximately, $\mu_{\mathbf{x}}$ and $\sigma_{\mathbf{x}}$ can be viewed as estimates of the stratigraphic sequences and structural variations in a local patch of model \mathbf{x} , and $\sigma_{\mathbf{xy}}$ measures the tendency of the patches in model \mathbf{x} and \mathbf{y} to vary together, thus an indication of structural similarity. β and γ define the relative significance of the two terms l and cs , which are both set to 1 based on Wang et al. (2003). In addition, we use two small constant factors C_1 and C_2 to avoid the numerically unstable circumstance of dividing by zero.

The standard deviation σ_g of the Gaussian filter G_{σ_g} is a hyper-parameter that requires to be defined before training. However, the choice of σ_g can impact the prediction accuracy of the network trained by using SSIM. The network trained by SSIM with a large standard deviation G_{σ_g} might overly emphasize the local variations and generate spurious features in the proximity of edges while blurring sharp structural boundaries for a small standard deviation G_{σ_g} (Zhao et al., 2016). Instead of fine-tuning the parameter G_{σ_g} , we use Multi-scale Structural Similarity (MS-SSIM) (Wang et al., 2003, 2004) with a dyadic pyramid of M scale levels and formulate it as follows,

$$\mathcal{L}_{\text{ms-ssim}}(\mathbf{p}) = 1 - l_S(\mathbf{p})^\beta \cdot \prod_{j=1}^S cs_j(\mathbf{p})^{\gamma_j}, \quad (3)$$

in which γ_j are parameters to define the relative importance of each scale level in the variance-related scheme cs_j . MS-SSIM computes a pyramid of patches \mathbf{p} with S spatial scales defined by various σ_g of the used Gaussian filter G_{σ_g} . We define 5 different scales of $\sigma_g = \{0.5, 1, 2, 4, 8\}$, and set each to half of the previous one by recursively downsampling the full-resolution patch using 2×2 average pool layer ($S = 5$). We adopt $\gamma_j = \{0.05, 0.29, 0.3, 0.24, 0.12\}$ to rescale the losses estimated from the 5 scale levels, and make sure the sum of them is equal to 1 for computing the MS-SSIM loss.

MS-SSIM highlights structural variations focusing on a neighborhood of point p as large as the given Gaussian filter G_{σ_g} , but might produce artefacts in the predictions because its derivatives cannot be correctly estimated near the boundary regions of the patch in the optimization. This can be alleviated by supplying an element-wise criterion that is computed on a single point of the patches being compared in the loss function. Additionally, MS-SSIM is not sensitive to uniform biases, which might cause unexpected changes in stratigraphic sequences or shifts of geological interfaces in modeling results. In comparison, although MAE can better preserve stratigraphic sequences by minimizing error at each point equally within the patch, it might not produce quite the same high-frequency contrast as MS-SSIM regardless of local structures. To capture the best characteristics of both loss functions, we thus propose to combine them as,

$$\mathcal{L}_{\text{sum}} = \frac{1}{K} \sum_{i=1}^K (\lambda \mathcal{L}_{\text{mae}}(\mathbf{p}_i) + \mathcal{L}_{\text{ms-ssim}}(\mathbf{p}_i)), \quad (4)$$

where λ is a weighting factor used to balance the relative importance of different losses, and K represents the number of cropped patches. In training the CNN, we point-wisely crop square patches from the structural models being measured and compute the loss within each patch based on Equation 4, in which we empirically set the dimensional size of each patch to 7 and the λ to 1.25. The total loss \mathcal{L}_{sum} is estimated by averaging the losses computed for the K patches. All the parameters in the loss function are selected based on many numerical experiments and kept fixed throughout the study to avoid the need for tuning. Although we cannot ensure the used parameter combination is the best one, further parameter tuning is much more time-consuming for training a deep CNN but hardly obtain further improvements.

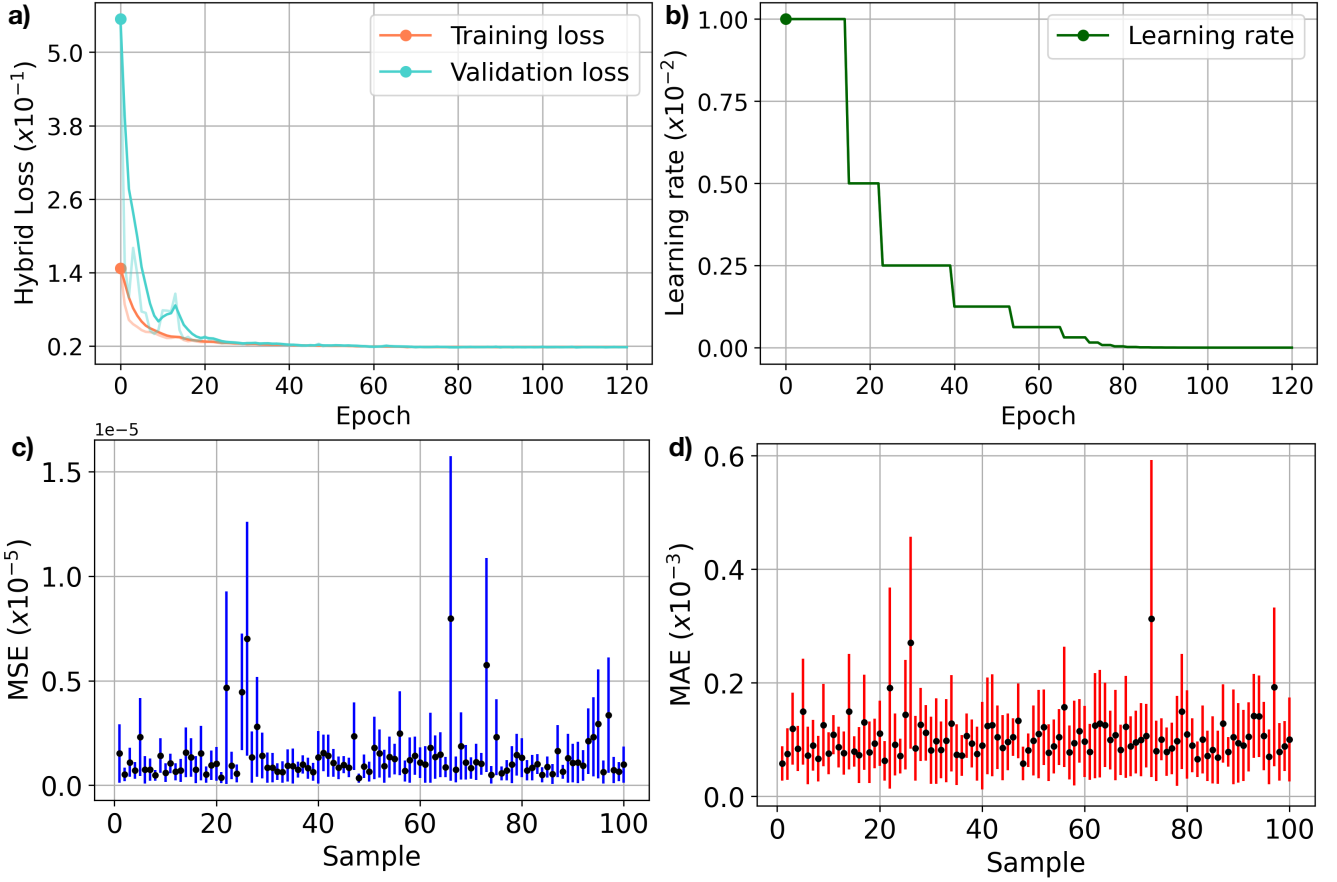


Figure 6. Training (cyan) and validation (orange) curves of using our developed hybrid loss (a), and the adaptive adjustment of the learning rate during the training (b). We run 20 times of the trained CNN to compute the MSE (c) and MAE (d) for the 100 models randomly chosen from the validation dataset, in which the input structural data are regenerated in each computation. The black dot represents the average error while the blue and red lines indicate the error ranges of the MSE and MAE, respectively.

255 3 DATA PREPARTION

Our CNN architecture is beneficial for the flexible incorporation of empirical geological knowledge in a supervised learning framework with numerous structural models that are all automatically generated from an automatic data simulation workflow. We randomly delete some segments from the models to obtain the partially missing horizons similar to the modeling objects collected from field observations. In training our network, the incomplete horizons, together with the faults, are used as inputs

260 to predict a structural scalar field under the supervision of the full model.

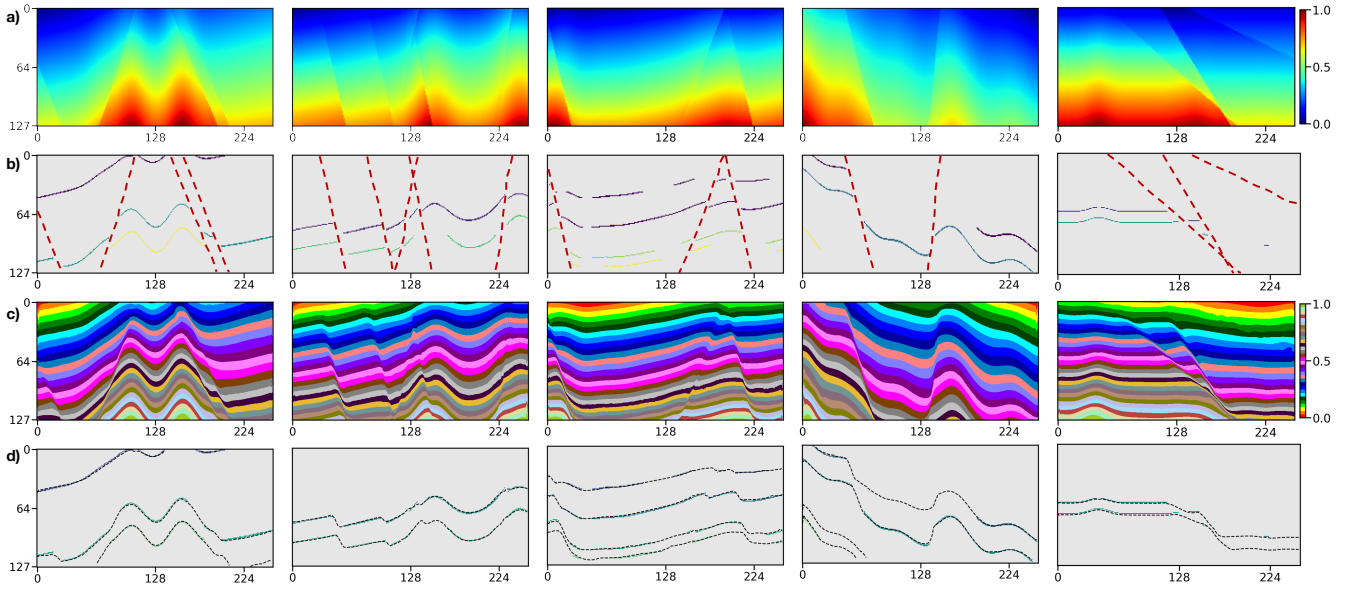


Figure 7. We apply the trained CNN to the 5 geological models (a) not included in the training dataset. We randomly generate horizon and fault structural data (b) from the models as the inputs of our network. By visual comparison, the modeling results (c) are nearly identical to the original models (a), which can be supported by the great consistency between the scalar field iso-lines (dashed curves) and the input horizons (solid curves) in (d).

3.1 Automatic Data Generator

A limitation of applying the supervised learning method is the preparation of many example data and especially the corresponding geological labels for training the network. In the structural modeling, the training dataset should incorporate structurally varying geological models as much as possible to enable the CNN to learn representative knowledge for achieving its reliable generalization in real-world applications. However, it is hardly possible to manually label all geological structures in a field survey because the ground truth of the subsurface is inaccessible. To overcome this problem, we use an automatic workflow to simulate geological structural models with some typical folding and faulting features that are controlled by a set of random parameters (Wu et al., 2020). In this workflow, we first create a flat layered model with horizontally constant and vertically monotonically increasing values as an initial model, and then sequentially add folding, dipping, and faulting structures to complicate the features of this model. We simulate the folding and dipping structures by vertically shearing the initial model through a combination of linear and Gaussian-like shift fields, while creating faulting structures by using volumetric vector fields defined around the fault surfaces. By randomly choosing the parameters within the reasonable ranges, we can simulate numerous geological models with diverse and realistic features not limited to a specific pattern. Based on the generated models with known structures, we can simply obtain the corresponding ground truth of the fault model with ones on faults and zeros elsewhere. These models can be viewed as the volumetric scalar functions as their iso-surfaces represent the corresponding

stratigraphic interfaces while the local value jumps indicate the structural discontinuities. This is important for our next step of constructing a training dataset to optimize our CNN for geological structural modeling. By using this workflow, we totally obtain 600 3-D structural models shown in Figure 4a, and each model contains $256 \times 256 \times 128$ grid points. These models are vertically flipped up-down and horizontally left-right to build an augmented dataset consisting of a total of 2,400 pairs of models. At the same time as vertically flipping models, we reverse the sign of their values to ensure that they vertically increase except across a reverse fault. As is shown in Figure 5a, we extract 4 evenly spaced slices along crossline and inline from the 3-D structural models, respectively, to further build a training dataset for the 2-D network. We use 90% of the datasets for training and the rest for validating the trained network.

3.2 Masked Structural Data

The input structural data of our network consists of scattered points that are gridded into a volumetric mesh with valid annotations on structures and zeros elsewhere. As is displayed in Figure 4b and Figure 5b, we label the points near the faults within one pixel to ones and zeros elsewhere to obtain the input fault data. To obtain the input horizon data, we set the points near the horizon surfaces within one pixel to the corresponding iso-values of the structural model, which ensures the points on the same horizon have consistent annotations. Furthermore, we randomly remove some points from the horizon data in each run of the data generation to simulate the unevenly distributed horizon interpretations from a field geological survey. To simulate the sparse and unevenly sampled horizon data, we randomly delete some segments from the model to simulate incomplete horizons in each run of data generation. The geological interfaces are implicitly embedded within the scalar field with the iso-values and can be obtained by iso-surface extraction methods.

As the geological interfaces are implicitly embedded in the scalar field with the iso-values and can be obtained by iso-surface extraction methods, we adopt Jittered sampling (Cook, 1986; Hennenfent and Herrmann, 2008) to randomly choose iso-values and compute their horizons. This sampling method benefits from remedying the deficiency of the regular sampling method that introduces a specific pattern in the inputs while preserving the beneficial properties of randomness. Specifically, we first sort all the iso-values into a uniformly spaced grid in descending order and then randomly extract one within each grid unit to compute the corresponding horizon. Thus, the horizons extracted from the structural model can be spatially varying and not spaced closely. To remove the points from the horizon data, the simplest method is to randomly generate many square patches and mask the scattered points within the patches. Although this method is commonly used for many image inpainting tasks (Yeh et al., 2017; Yu et al., 2018b), it might negatively impact the CNN to be well generalized in real-world applications for which the inaccessible regions are unlikely in the shape of squares. To solve this issue, we randomize this process by randomly removing points from an individual horizon to prevent the network from learning a specific pattern that all the horizon data are partially missing in the same square regions. Similar to the iso-value selection, we first sort the points on this horizon into a uniformly spaced grid in descending order based on their vertical coordinates, and then randomly mask out the points from one or more grid units. As is displayed in Figure 4c and Figure 5c, the generated partially missing data are similar to the horizons manually interpreted by geologists and geophysicists, which enables the CNN to learn more representative features. Thus, we use this masking method for all the 2-D and 3-D synthetic data experiments in this study.

3-D Network architecture		Computational cost		Modeling quality metric							
Name	Backbone	GFLOPs	#Params[MB]	SSIM	EVS	MAE	MSE $\times 10^{-1}$	MSLE $\times 10^{-1}$	R2S	MDAE	HFA
UNet	-	32.715	34.526	0.989	0.990	0.019	0.009	0.005	0.972	0.017	1.078
AttUNet	-	33.265	34.878	0.981	0.978	0.027	0.035	0.018	0.901	0.025	1.029
NestUNet	-	76.406	39.091	0.839	0.773	0.129	0.250	0.126	0.288	0.115	3.025
DeepLabv3 ⁺	Xception	10.328	54.510	0.988	0.990	0.194	0.008	0.004	0.977	0.017	1.634
DeepLabv3 ⁺	DRNet54	23.293	40.672	0.989	0.991	0.019	0.008	0.004	0.978	0.018	1.228
DeepLabv3 ⁺	ResNet101	11.042	59.226	0.986	0.985	0.024	0.014	0.007	0.956	0.022	1.623
DeepLabv3 ⁺	MobileNetv2	4.364	7.555	0.985	0.982	0.027	0.017	0.008	0.949	0.025	1.843
RefineNet	MobileNetv2	1.015	3.250	0.973	0.963	0.031	0.035	0.019	0.887	0.028	1.223
RefineNet	MobileNetv3	0.937	2.600	0.977	0.981	0.030	0.022	0.011	0.937	0.028	1.735
DeepISMNet*	-	4.711	4.300	0.993	0.996	0.016	0.004	0.002	0.988	0.015	0.331

Table 1. A quantitative comparison between our network and the widely used powerful networks using various quality metrics. For each of the quality metrics, the best performance is highlighted in **bold**. The proposed network (DeepISMNet) is marked with an asterisk to distinguish it from the others.

Loss function	Modeling quality metrics						
	MAE	MSE $\times 10^{-1}$	EVS	R2S	MDAE	SSIM	HFA
L1	0.017	0.005	0.994	0.986	0.016	0.991	0.527
L2	0.017	0.005	0.995	0.987	0.016	0.989	1.321
SmoothL1	0.017	0.005	0.995	0.988	0.017	0.990	0.511
SSIM	0.017	0.006	0.992	0.978	0.018	0.989	0.643
MS-SSIM	0.017	0.005	0.994	0.986	0.016	0.991	0.630
MS-SSIM&L1	0.016	0.004	0.996	0.988	0.015	0.993	0.331
MS-SSIM&L2	0.016	0.004	0.995	0.987	0.015	0.990	1.040

Table 2. A quantitative analysis of our network trained with the distinct loss functions using multiple modeling quality metrics. For each of the quality metrics, the best modeling result is highlighted in **bold**.

310 4 IMPLEMENTATION

We present the geological structural models derived from our CNN for both synthetic data examples and field data applications in this section to demonstrate its modeling performance.

4.1 Training and Validation

315 Considering the coordinate ranges of the field geological datasets can be much different from each other, we rescale every structural model to obtain the normalized one that ranges from zero to one. This normalization is implemented by first sub-

tracting the minimum and then dividing its maximum and thus would not change its geological structures. When normalizing the structural data, we assign the scattered points on the same geological interface to the corresponding iso-values of the normalized model. In training the network, we formulate these normalized training samples in batches and set the batch size to 4 based on our computational resources. Within each epoch, the training data are all passed throughout the network to compute the hybrid loss function. We utilize Adam optimization (Kingma and Ba, 2014) with an adaptive learning step length to speed up the network optimization. The initial learning rate is set to 0.01, which reduces gradually when the criterion performance has stopped further improving. We fold the learning rate by a factor of 0.5 once the loss stagnates within 2 iterations. As is shown in Figure 6a, the training and validation loss curves gradually converge to low levels (less than 0.1) when the optimization stops after 120 epochs, which demonstrates that the CNN has learned representative geometries and relationships of geological structures from the training dataset. The learning rate is adaptively adjusted as is displayed in Figure 6b during the training process.

Furthermore, we evaluate the modeling stability of our network in terms of the perturbations of the input structures created from the same geological model. In this experiment, we randomly choose 100 synthetic models from the validation dataset and run 20 times of the trained network to calculate the MSE and MAE for each model. During each modeling process, we randomly generate the horizon scattered points to ensure that the input data are different from each other even for the same structural model. We show the variations of MSE and MAE for each model in Figure 6c and 6d, respectively, in which the MSE and MAE are represented by black dots while the error ranges are denoted by the blue and red lines. As is displayed in Figure 6, we can observe that most MSE and MAE are less than 0.5×10^{-5} and 0.2×10^{-3} , which are considered to be not very significant in geological modeling scenarios. This demonstrates the proposed CNN architecture is beneficial for implicit structural modeling.

4.2 Synthetic Data Examples

When the CNN is well trained, the modeling experiences and knowledge learned from the synthetic dataset are implicitly embedded in the network parameters. To verify its modeling performance, we apply the trained CNN to the 5 synthetic structural models not included in the training dataset. As is shown in Figure 7a, the models are of complex faulted layered volumes, in which the folded interfaces are reformed by multiple high-angle normal faults. From the original structural models, we generate the incomplete horizon and the fault data (Figure 7b) used as inputs of our network. By visual comparison in Figure 7c, the modeling results with similar geometrical features to the inputs maintain the localized variations of the folded interfaces despite no global structural information used to constrain the model. We further overlap scattered horizon points on the iso-lines of the field predictions (Figure 7d), in which the great consistency between the given structures and the interpolated features again supports our observation in Figure 7c.

As is tabulated in Table 1, the CNN’s modeling ability is quantitatively measured by using various quality metrics including SSIM, MSE, MAE, Explained Variance Score (EVS), Mean Squared Log Error (MSLE), Median Absolute Error (MDAE), and R Square Score (R2S) on the entire validation dataset. In addition, we also measure the modeling accuracy of every geological interface related to the input horizon data by computing Horizon Fitting Error (HFA). This metric measures an

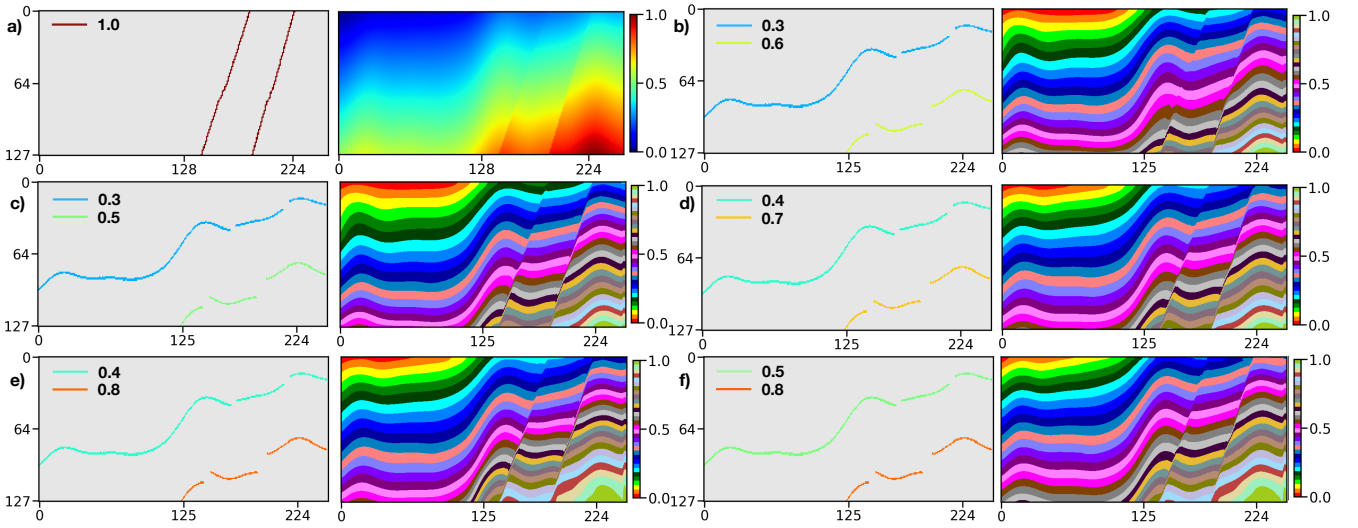


Figure 8. We use a synthetic model (a) to study how the varying horizon values impact the CNN’s modeling results. The experiments are used to verify that our network can produce almost identical structural models from the same faults and the horizons with varying values, as shown from (b) to (f). This indicates that our approach is not sensitive to the annotation assigned to each horizon in the input structural data, which facilitates its applications in field surveys.

average distance between the horizon scattered points and the corresponding iso-surfaces of the predicted model along the vertical axis. Table 1 also shows a quantitative comparison of the proposed method (DeepISMNet) and the other powerful networks commonly used in similar scenarios. Our method not only shows better performance on all the metrics but also has a more lightweight architecture with fewer trainable parameters and GFLOPs in comparison to other CNNs. Simplification of the network architecture is mainly associated with the use of inverse residual modules followed by depth-wise separable convolutions in each spatial scale level throughout the network, enabling our CNN to be applied to a large 3-D field modeling task. To guarantee the representational ability of the simplified CNN, the channel-wise dependencies have been explicitly learned by using an attention module that can adaptively highlight more informative features while suppressing irrelevant ones. Therefore, although the number of hidden representations is less than the conventional CNN architectures such as UNet, our network can still achieve stable structural interpolation and reliable generalization performance.

5 APPLICATION

It might not be surprising that the CNN trained with a synthetic dataset works well to produce a geologically valid and consistent model by using the structural data created from the same workflow for creating the training dataset. In this section, we further present structural modeling results from our trained network for real-world data that are acquired at different geological surveys to demonstrate proof of concept. The modeling objects collected from field observations or seismic data are required to convert into the uniformly sampling grids to obtain the input structural data of our CNN.

5.1 Structural Data Preprocessing

In most cases, the structural data collected from field surveys are discrete and not necessarily located on the sampling grid of the model, such that we need a preprocessing step that scatters the structural data into a volumetric mesh with annotations. To scatter the structural data, we simply shift the horizon and fault interpretations to their nearest sampling grids of the model and obtain the associated scattered points. In both the synthetic and the field data applications, the annotation of fault scattered points is straightforward by simply assigning ones near the faults and zeros elsewhere. However, although the points along the horizons can be assigned to the corresponding iso-values of the model in the synthetic data experiments, this might not be feasible when modeling real-world geology from structural interpretations.

As the ground truth of geological structures is typically inaccessible before modeling, how to properly annotate the interpreted horizons remains a problem. We implement a numerical experiment using the horizon data labelled with different iso-values in a synthetic structural model (Figure 8a) to study how they impact the predictions of our CNN. In this experiment, the scattered points on two horizons are assigned by the normalized iso-values that range from 0.3 to 0.8 with three distinct intervals of 0.2, 0.3, and 0.4. As shown from Figure 8b to 8f, the network takes the horizon data with various iso-values and the same fault data to produce structural models as outputs. By visual comparison, the nearly identical modeling results indicate that the method is not sensitive to the different data annotations within a reasonable range, which is what we expect. Additionally, we can observe that a larger interval of the horizon annotations is contributed to a more significant displacement of geological layers on the opposite of the fault structures in the predicted model (Figure 8c and 8e). Based on this observation, we recommend labeling the scattered points on each horizon with their average vertical coordinate to correctly model the stratigraphic sequences of geology. Note that the annotations on horizons require to be consistently rescaled by the model size to keep consistent with the normalized training dataset.

5.2 Real World 2-D Case Studies

We apply the trained CNN to 2-D field data to verify its modeling performance for the structural data with geometrical patterns distinct from the training data. The input structural data are manually interpreted from the seismic images that are acquired from the Westcam dataset. This dataset is acquired in regions with closely spaced and complexly crossing faults with large slips, in which the seismic images are of low resolution due to insufficient coverage and data stacking. The ambiguous seismic reflections shown in Figure 9a are difficult to be continuously tracked across the entire seismic images, which causes the partially missing horizon data displayed by different colors in Figure 9b. The faults also might not be fully detected from the seismic images in the presence of data-incoherent noise and the stratigraphic features that are similar to structural discontinuities. Moreover, the structural contradictions and hard-to-reconcile features in the structural data might negatively impact the modeling performance of the implicit methods. Thus, there remains a challenging task for many traditional approaches to obtain a geologically reasonable model that is structurally consistent with the inputs.

As is shown in Figure 9d, our method presents geologically valid models (Figure 9d) with the structural discontinuities and the stratigraphic interface variations that consistently honor the faults and horizons, respectively. From Figure 9e, we observe

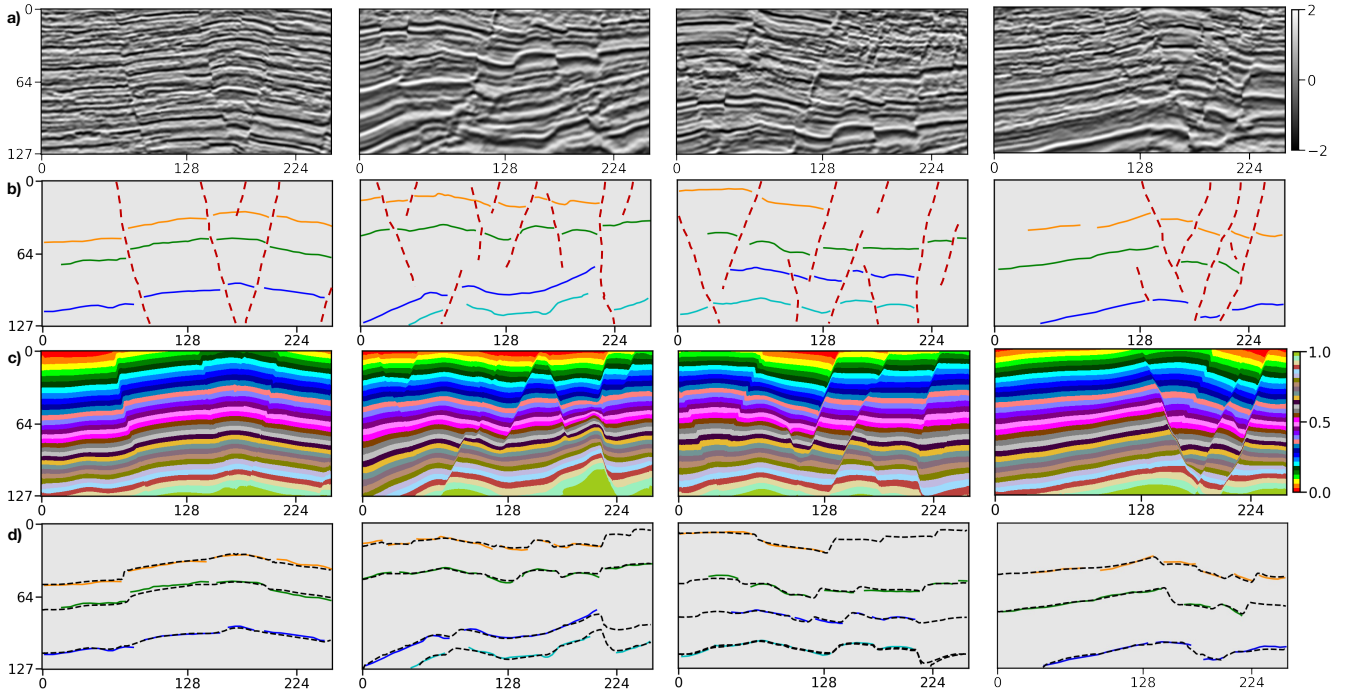


Figure 9. Application in a seismic field dataset. We display seismic images (a), input structural data (b) interpreted from the seismic images, predicted structural models (c), and horizon fitting results (d), respectively.

that the iso-lines (black lines) extracted from the modeling results can accurately follow the horizon interpretations in Figure 9b, which again supports our previous observation. In comparison to the scattered point-sets, a full structural model is more useful to well understand geological structures and qualify reservoir properties of continuity and morphology. Furthermore, the deep learning method with high computational efficiency can even produce real-time predictions to correct interpretation errors and improve the geological consistency of the model by taking all the structural interpretations into account.

The second 2-D field data experiment uses the dataset acquired from a geological survey and mineral exploration of the Araripe Basin in the region of the Borborema Province of Northeastern Brazil (Fabin et al., 2018). We collect the outcrop observations shown in Figure 10a and 10f from exposures of quarries on the southwestern and northern borders of the basin. There exist a series of moderate to high angle faults caused by local subsidence due to the syn-depositional dissolution of the gypsum in a large exposure of deposits of the Romualdo Formation. These syn-depositional faults control the lateral thickness variations of the stratigraphic interfaces that the field observations sample from outcrops. The field observations are integrated into the uniform sampling grids and used as inputs of our trained CNN to predict a full structural model. As is displayed in Figure 10b and 10g, the dataset incorporates four stratigraphic interfaces with three and four faults, respectively, exhibiting a structural pattern of syn-depositional deformation that is not included in our training dataset.

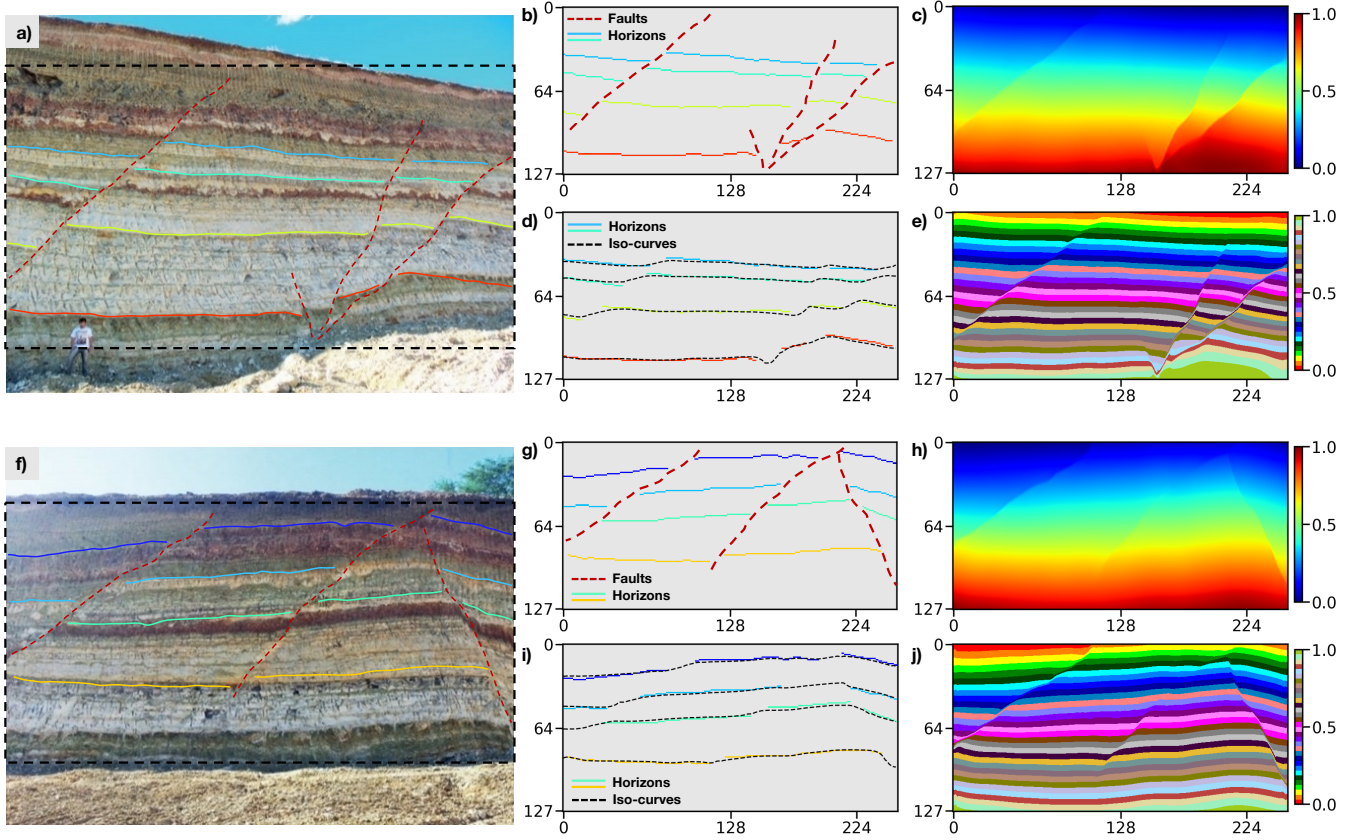


Figure 10. Application in an outcrop field dataset. We display two outcrop images (Fabian et al., 2018) in (a) and (f), input structural data in (b) and (g) manually interpreted from the outcrop images within the dashed boxes, predicted structural models using a continuous color map in (c) and (h), and a discrete color map in (e) and (j), and horizon fitting results in (d) and (i), respectively.

The modeling results presented in Figure 10c and 10h are obtained from the trained CNN, in which all the sharp edges are structurally consistent with the faults shown in Figure 10b and 10g, respectively. The same structural models can be displayed in Figure 10e and 10j using a discrete color map to indicate dislocated stratigraphic layers on the opposites of the faults. The iso-lines extracted from the modeling results for the four distinct horizons are shown in Figure 10d and 10i, respectively. Both figures highlight the excellent fitting characteristic of the trained CNN on the input structural data. Therefore, although the CNN is trained with the automatically simulated data, it still provides a promising performance on the real-world dataset acquired at totally different surveys with complex geological structures.

5.3 Real World 3-D Case Studies

Using the automatically simulated dataset, we train a 3-D modeling network with the same architecture as the 2-D CNN above to correctly capture the geometrical characteristics of 3-D geology. To validate its modeling ability, we apply the trained CNN

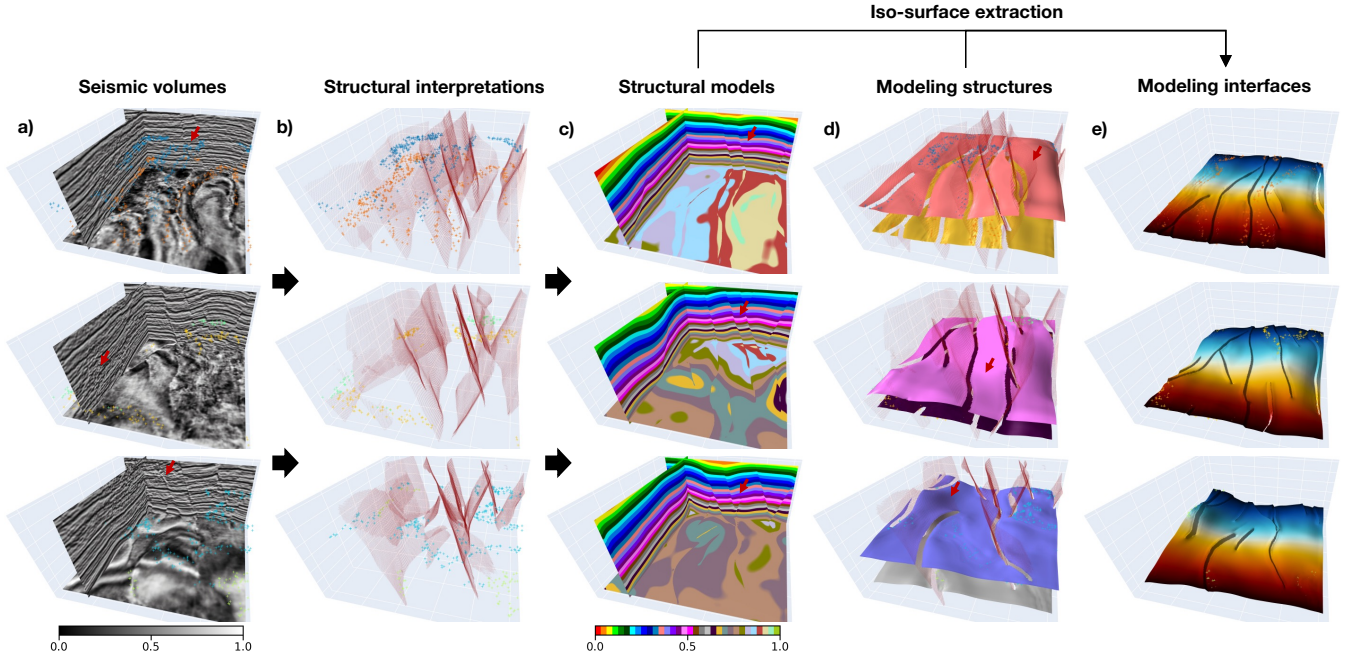


Figure 11. The first real-world data application. We display seismic volumes (a), input horizon and fault data interpreted from the seismic volumes (b), modeling results (c), geological interfaces extracted from the modeling results and overlaid with the faults (d), and one of the recovered full horizon surfaces(e), respectively.

to 3-D field data and construct a full structural model from unevenly sampled scattered points obtained from seismic interpretation. The first seismic data sampled in regions with complexly deformed structures have relatively low resolution and signal-to-noise ratio. As is shown in Figure Figure 11a, some seismic reflections are noisy and difficult to be continuously tracked across the entire volume of interest. The closely spaced and crossing faults further complicate the geometries of structures especially when there exists data-incoherent noise and stratigraphic features that are similar to structural discontinuities (highlighted by arrows in Figure 11a). In addition, the scattered points heterogeneously sampled around the geological interfaces (Figure 11b) are sparse or clustered in some localized regions because of the large variations in the distances between the points.

The modeling results shown in Figure 11c demonstrate that the CNN architecture is beneficial for 3-D structural modeling by predicting a geologically valid model, where the structural discontinuities and the interfaces are consistent with the given points (Figure 11d). The predicted models even maintain the variations of the folded layer structures (highlighted by arrows in Figure 11c and 11d) without global plunge information used to constrain the modeling process. By visual comparison, Figure 11c shows that a group of horizon points sampled at the same geological layer can be accurately located on the corresponding iso-surface of the model, which again demonstrates a great fitting characteristic of our network.

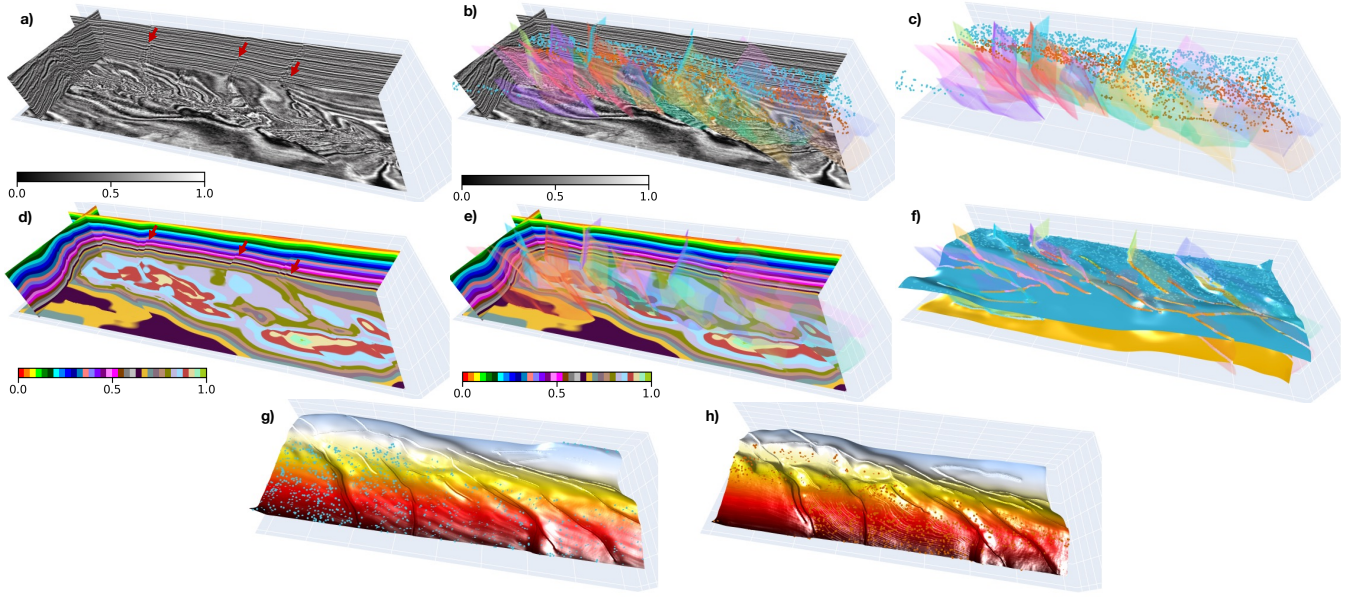


Figure 12. The second real-world data application. We display seismic volume (a) overlaid with structural data (b), input horizon and fault data (c) interpreted from the seismic volume, modeling result (d) overlaid with faults (e), geological interfaces extracted from the modeling result (f), and each of the recovered full horizon surfaces in (g) and (h), respectively. Noting that we rotate the horizon surfaces (g) and (h) by 180° for a better visual comparison.

The second 3-D real-world case study is of a conformably folded and layered model with numerous faults that are curved and complexly intersected with each other. As is shown in Figure 12a, the available horizon data are manually interpreted on the two stratigraphic interfaces, while the fault data are derived by using the automatic fault detection method from the seismic volume (Figure 12b and 12c). In our CNN's prediction shown in Figure 12d, the geological layers represented by iso-values with the same color accurately follow the tendency of seismic structural variations near the faults (highlighted by arrows in Figure 12a and 12d) even though we do not input any seismic data in our CNN. We also display the modeling result overlaid with the input fault data in Figure 12e, from which we can observe dislocations of geological layers on the opposites of the fault structures (highlighted by arrows in Figure 12e). In Figure 12f, we extract the geological interfaces that correspond to the input horizons using the iso-surface extraction approach. To show more details, Figure 12g and 12h display each of the horizon surfaces, by which we rotate 180° for a better visual comparison. A great consistency between the input and recovered structures highlights the CNN's fitting characteristics on the given geological knowledge and structural constraints.

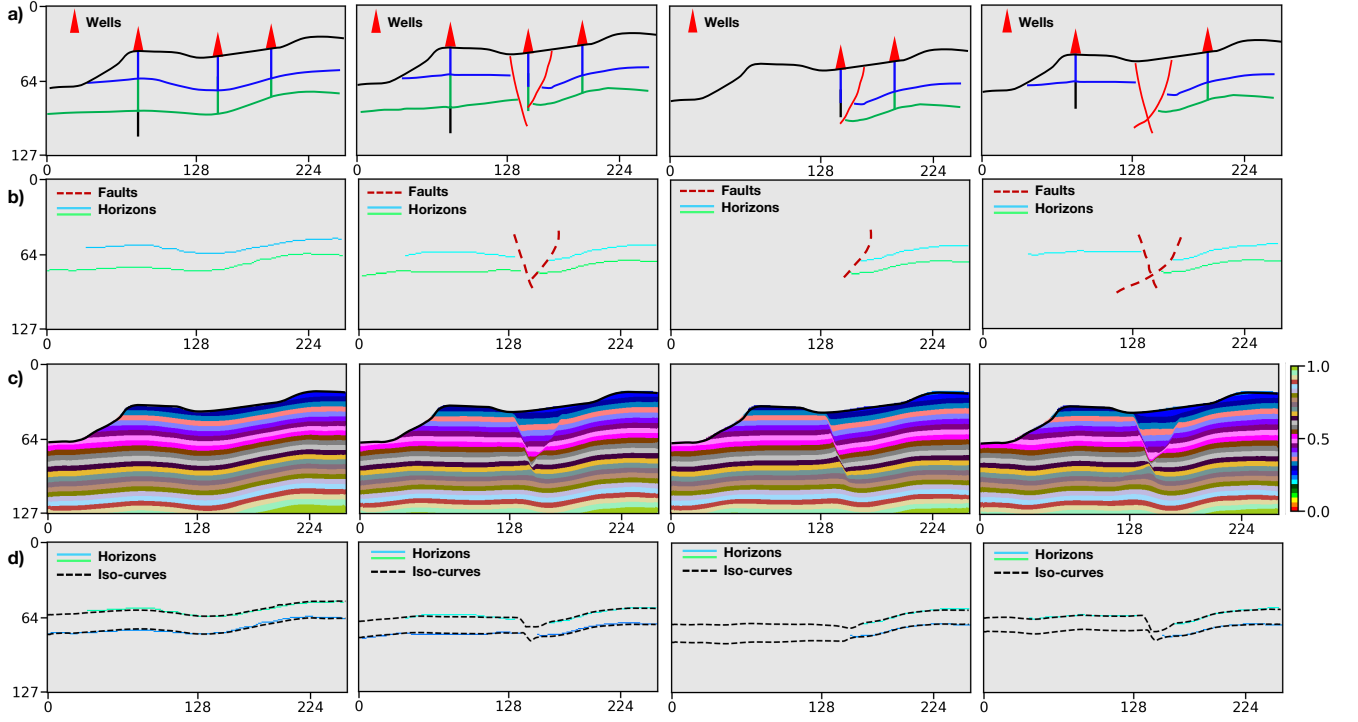


Figure 13. Geological uncertainty analysis. We display multiple sets of modeling elements interpreted from the borehole and the outcrop observations (a), input horizon and fault data (b), modeling result (c), and iso-curves extracted from the prediction (d), respectively.

6 DISCUSSION

In this section, we discuss the modeling characteristic of our method and its abilities for structural uncertainty analysis, along with the current limitations. We also demonstrate a potential improvement that we will focus on in future research to incorporate structural orientation constraints in the CNN-based structural modeling.

6.1 Structural Uncertainty Characterization

When modeling complex geological structures, the reliability of the implicit methods is heavily dependent on the quality and availability of the input structural data. However, the heterogeneously distributed structural data pose an ill-posed problem that there exist multiple plausible structural models which equally fit the inputs. However, the inputs typically sparse and regional available in a geological survey cause an ill-posed problem because there exist multiple plausible resultant models that equally fit the inputs. Therefore, data uncertainty analysis is necessarily critical to looking for an optimal solution, especially for the noisy and hard-to-reconcile structural observations (Viard et al., 2011; Lindsay et al., 2012). Although the existing implicit methods can generate various models by perturbing the inputs to characterize uncertainties, they might not explore a broad range of possible geological patterns and structural relationships in nature through a single model suit for stochastic simula-

tion (Jessell et al., 2022). Working on the automating of modeling workflow, our CNN is beneficial for a flexible interpretation of aleatory and epistemic uncertainties (Piriot et al., 2022) by generating diverse modeling realizations instead of one best due to its high computational efficiency.

We can use various combinations of modeling objects with the horizons and faults interpreted from the borehole and the outcrop observations shown in 13a to study the uncertainties associated with the position variations of geological structures. The model with the simplest structures consists of multiple continuous and conformal geological layers shown in the first data example. The modeling situations become more complex and various when considering additional geometrical objects such as faults or unconformities to dislocate the continuous layers. Furthermore, we randomly perturb the interpreted geological interfaces to yield the variations of layer thickness as the stratigraphic boundary transition often might not be accurately observed from the vertical boreholes. As is shown in Figure 13b, the network takes a diverse set of combinations to model the possible structural geometries and relationships to demonstrate proof of concept. All the results are computed by using a desktop PC with Intel Xeon-5120 CPU (2.20GHz) and a single NVIDIA Tesla V100 GPU. Although we take a few hours in training the CNN, the average time for generating each model is approximate 0.2 seconds using a 128×256 image size. We display the iso-curves of the models (Figure 13c) overlaid with the horizons in Figure 13d, which verifies an excellent fitting characteristic of our approach on the given geological structures.

6.2 Structural Orientation Constraint

Our CNN architecture permits the flexible incorporation of varying types of geological information by defining an appropriate loss function to measure the modeling error for each structural constraint. In our method, the input data are not limited to horizons and faults and can include the structural angular observations in the modeling process. We can use the structural angular information that represents local orientations of geological layers to permit geometrical relationships in the gradient of the scalar function to be considered. The loss function of orientation constraint is aimed to measure the angle errors between the directional derivatives of the predicted model and the orientation observations using cosine similarity. We adopt the second-order accurate central differences method (Fornberg, 1988) using the Taylor series approximation to estimate the local orientation at each interior point of the given structural model \mathbf{z} . The cosine similarity at every single point between the orientations of the predicted model and the normal vector $\vec{\mathbf{n}}$ can be represented as follows,

$$f_{cs}^{\text{pred}}(p) = \frac{\vec{\mathbf{n}} \cdot \nabla \mathbf{z}(p)}{\|\vec{\mathbf{n}}\| \|\nabla \mathbf{z}(p)\|}. \quad (5)$$

This is also used to compute the cosine similarity between the orientations in the reference model $f_{cs}^{\text{obs}}(p)$ and the normal vector \mathbf{n} . Therefore, the loss function that measures the structural angle errors between the two models being compared can be formulated as follows,

$$\mathcal{L}_{\text{normal}}(\mathbf{p}) = \frac{1}{N} \sum_{p \in \mathbf{p}} |f_{cs}^{\text{pred}}(p) - f_{cs}^{\text{obs}}(p)|, \quad (6)$$

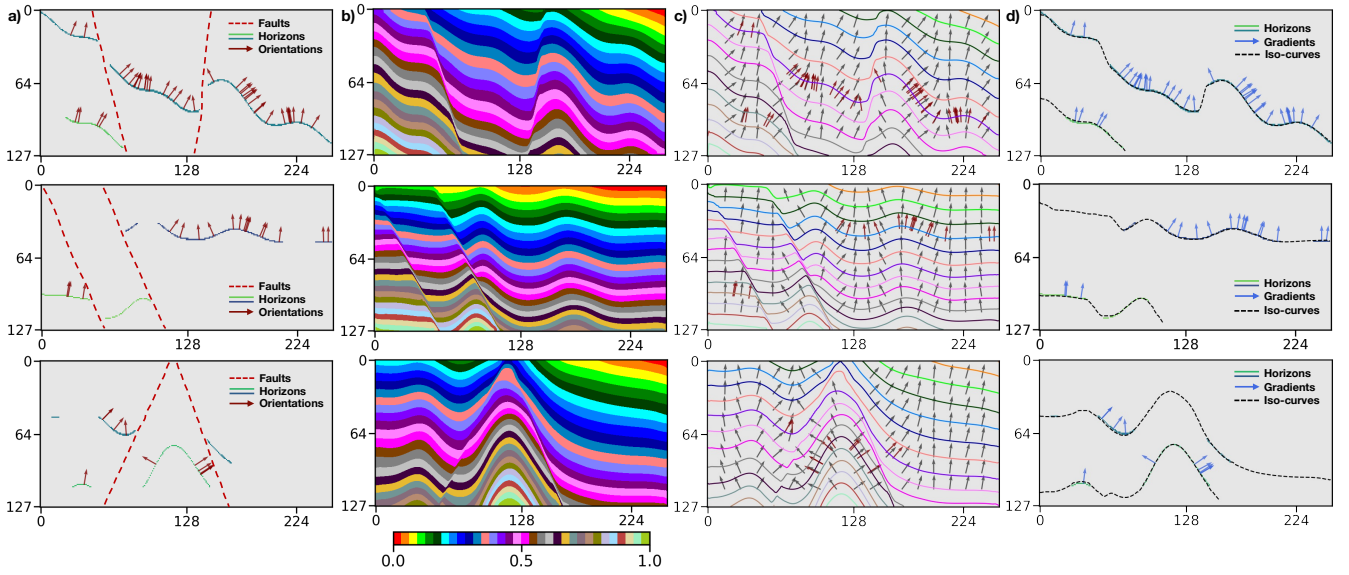


Figure 14. The faults and incomplete horizons, together with the structural orientations, are used as inputs (a) into the network to predict implicit structural models (b). The sets of regularly spaced iso-lines and local orientations are obtained from the modeling results (c) and compared with the given normal vectors (red arrows). The iso-lines and normal vectors (blue arrows) extracted on the predicted stratigraphic interfaces can well match the two distinct input horizons (d).

in which N represents the total number of the points within a patch \mathbf{p} . Therefore, the total loss function is defined by combining the various types of geological constraints as,

$$\mathcal{L}_{\text{sum}}(\mathbf{p}) = \frac{1}{K} \sum_{i=1}^K (\lambda \mathcal{L}_{\text{mae}}(\mathbf{p}_i) + \mathcal{L}_{\text{ms-ssim}}(\mathbf{p}_i) + \beta \mathcal{L}_{\text{normal}}(\mathbf{p}_i)), \quad (7)$$

where β is used to balance the relative significance of the orientation loss, and K represents the number of the patches cropped from the model. β and λ are empirically set to 1.00 and 1.25, respectively, according to many prior numerical tests. As is displayed in Figure 13a, the faults and the incomplete horizons, together with the structural orientations sparsely distributed on the horizons, are used as inputs to the network to model geological structures. The modeling results shown in Figure 13b exhibit the remarkable performance of our method when using various types of geological data inputs. We compute regularly spaced iso-lines and local orientations from every modeling result and compare them with the input normal vectors (red arrows) in Figure 13c, respectively, which presents a great consistency between the predicted and given geological structures. The interpolated structures by using the CNN maintain the large localized geometrical variations even though there is no global geological information to constrain the modeling process. In addition, the iso-lines and normal vectors (blue arrows) extracted along the stratigraphic interfaces of the predictions can well match the two distinct input horizons (Figure 13d), which again highlights the CNN's fitting characteristic on the given structural constraints.

The CNN trained by using the synthetic dataset presents excellent modeling capacities in real-world cause studies to represent complicated geological structures that are distinct from the simulated structural models. Instead of imposing any explicit mathematical constraints in the traditional implicit method, our CNN-based structural modeling is implemented by the recursive spatial convolutions with trainable kernel parameters and the loss function related to various geological constraints. The spatial convolutions in the CNN can be viewed as the implicit interpolants used in the traditional interpolation methods, and the only difference is that the parameterization of their kernel functions can be optimized through training. As structural modeling is dependent on the analysis of the spatial relations of the observed structures to interpolate new geologically valid structures elsewhere, acquiring representative example data is essential for training the CNN to achieve its reliable generalization performance. Therefore, we adopt an automatic workflow to generate numerous models with realistic structures and simulate partially missing horizons in building the training dataset. It is a significant reason why our network could be applied to the real-world datasets acquired in different geological surveys with distinct structural patterns.

Another improvement of our approach is attributed to the use of a loss function based on element-wise accuracy and structural similarity in updating the CNN's parameters. To demonstrate the improved modeling performance, we implement a quantitative analysis of our CNN trained with the different loss functions using the multiple quality metrics. The averages of these metrics on the validation dataset are tabulated in Table 2. The CNN trained with the hybrid loss function of MS-SSIM and MAE (denoted by MS-SSIM&L1) can outperform the others in Table 2 on all the quality metrics even including the quality metrics which we use as cost function to train the network. This loss function is attributed to a better reconstruction of fault-related features in the resultant model by assigning high weights to regional structural contrasts. Also, reliable identification of faults is useful to constrain the lateral occurrence of stratigraphic interfaces across structural discontinuities.

Although working well to recover faulted and folded structures, the proposed method might not represent other geological structures that are not considered in the training dataset, such as unconformities and igneous intrusions. The trained network also might not correctly construct low dip-angle thrust faults in predicted models because we still do not include this type of fault in the currently used data generator. Despite the current limitations, the proposed CNN architecture still shows promising potential to compute a geological valid and structurally consistent model honoring the observed structures. Considering the used training dataset is still not sufficiently large to train a 3-D deep network, future works will focus on expanding our training dataset to a broader range of geological geometries and relationships. For example, we can further complicate the used simulation workflow by adding more complex and diverse features in the structural models, or adopting a recently developed 3-D geological modeling dataset (Jessell et al., 2022) where dykes, plugs, and unconformities are incorporated.

7 Conclusions

A CNN-based deep learning method has been used to represent geological structures over the entire volume of interest from typically sparse and hard-to-reconcile structural interpretation data. The network is composed of encoder and decoder branches and supplemented with lightweight depth-wise separable convolution and channel-wise attention to find an optimal trade-off

between modeling accuracy and computational efficiency. The developed CNN architecture leverages the low-rank nature of the sparse and heterogeneously sampled structural data to adaptively suppress uninformative features by using a linear bottleneck and inverted residual structure in each of the encoded convolutional layers. Our approach is beneficial for the flexible incorporation of empirical geological knowledge constraints in a supervised learning framework using numerous and realistic structural models that are generated from an automatic data simulation workflow. This also provides an impressive characteristic to flexibly integrate multiple types of structural constraints into the modeling by using an appropriate loss function, exhibiting a promising perspective for further improving geological modeling. We verify the effectiveness of the proposed approach by using the case studies acquired in distinct geological surveys, including synthetic examples created by the same workflow for acquiring the training dataset, the randomly created modeling objects without any ground truth of geology, and the structural interpretations obtained from the seismic images. In both synthetic data and real-world data applications, we verify its modeling capacities in representing complex structures with a model geologically reasonable and structurally consistent with the inputs.

Code and data availability. The synthetic structural models, used for training and validating our network, are uploaded to Zenodo and are freely available through the DOI link <https://doi.org/10.5281/zenodo.6480165>. The source codes for the neural network developed in Pytorch are uploaded to Zenodo and provided at the DOI link <https://doi.org/10.5281/zenodo.6684269>.

Appendix A: Regression metric functions

To verify the modeling performance of our CNN, we quantitatively measure the differences between the ground truth structural models and predictions by using various regression metrics including SSIM (Structural Similarity), MSE (Mean Square Error), MAE (Mean Absolute Error), EVS (Explained Variance Score), MSLE (Mean Square Logarithm Error), MDAE (Median Absolute Error), and R2S (R Square Score, also called the Coefficient of Determination) in the validation dataset. MSLE measures the prediction performance that corresponds to the expected value of the squared logarithmic error, which is formulated as,

$$f_{\text{MSLE}}(\mathbf{y}, \hat{\mathbf{y}}) = \frac{1}{N} \sum_{i=1}^N (\log_e(1 + \mathbf{y}_i) - \log_e(1 + \hat{\mathbf{y}}_i))^2, \quad (\text{A1})$$

where \mathbf{y} and $\hat{\mathbf{y}}$ are the structural models being measured, respectively, and N represents the total number of points in the model. MDAE is computed by using the median of all absolute differences and thus can be robust to outliers,

$$f_{\text{MDAE}}(\mathbf{y}, \hat{\mathbf{y}}) = \frac{1}{N} \sum_{i=1}^N \text{median}(\mathbf{y}_i - \hat{\mathbf{y}}_i). \quad (\text{A2})$$

EVS is used to measure the proportion of the variability of the solutions in a machine learning method, and the score value ranges from zero to one. Higher EVS typically indicates a stronger strength of association between regression targets and predictions and thus represents better network performance. It can be formulated as follows,

$$f_{\text{EVS}}(\mathbf{p}) = \frac{1}{M} \sum_{p \in \mathbf{p}} \left(1 - \frac{\text{variance}(\mathbf{y} - \hat{\mathbf{y}})}{\text{variance}(\mathbf{y})}\right), \quad (\text{A3})$$

where \mathbf{p} represents the patch cropped from the same spatial location from the structural models being measured, and M is the number of the cropped patches. R2S offers a measurement of how well the predictions of the network are based on the proportion of total variations. R2S can be written as follows,

$$f_{\text{R2S}}(\mathbf{p}) = \frac{1}{M} \sum_{p \in \mathbf{p}} \left(1 - \frac{\sum_{i=1}^N (\mathbf{y} - \hat{\mathbf{y}})^2}{\sum_{i=1}^N (\mathbf{y} - \bar{\mathbf{y}})^2}\right), \quad (\text{A4})$$

in which N represents the total number of points within the cropped patch \mathbf{p} . R2S is similar to EVS, with the notable improvement that it can account for systematic offsets in the predictions. In addition, EVS and R2S can be more robust and informative than MAE and MSE in regression analysis evaluation because the former can be represented as percentage errors.

Author contributions. XW initiated the idea of this study and advised the research on it. ZB conducted the research and implemented the 2-D and 3-D CNN-based structural modeling algorithms. XW conducted numerical structural simulations to provide synthetic structural models for training. ZB prepared the training datasets from the simulated structural models and carried out the experiments for both synthetic and real-world case studies. ZL, DC, and XY helped design the experiments and advised on result analysis from a geological perspective. ZB and XW prepared the manuscript with contributions from all co-authors.

Competing interests. The authors declare that they have no conflict of interest.

Acknowledgements. This research is financially supported by the National Science Foundation of China under grant no. 42050104 and Research Institute of Petroleum Exploration & Development-NorthWest (NWGI), PetroChina.

References

- Alon, U. and Yahav, E.: On the bottleneck of graph neural networks and its practical implications, arXiv preprint arXiv:2006.05205, 2020.
- Bi, Z., Wu, X., Geng, Z., and Li, H.: Deep relative geologic time: a deep learning method for simultaneously interpreting 3-D seismic
585 horizons and faults, *Journal of Geophysical Research: Solid Earth*, 126, e2021JB021 882, 2021.
- Calcagno, P., Chilès, J.-P., Courrioux, G., and Guillen, A.: Geological modelling from field data and geological knowledge: Part I. Modelling method coupling 3D potential-field interpolation and geological rules, *Physics of the Earth and Planetary Interiors*, 171, 147–157, 2008.
- Carr, J. C., Beatson, R. K., Cherrie, J. B., Mitchell, T. J., Fright, W. R., McCallum, B. C., and Evans, T. R.: Reconstruction and representation of 3D objects with radial basis functions, in: *Proceedings of the 28th annual conference on Computer graphics and interactive techniques*,
590 pp. 67–76, 2001.
- Caumon, G., Collon-Drouaillet, P., Veslud, C. L. C. D., Viseur, S., and Sausse, J.: Surface-based 3D modeling of geological structures, *Mathematical Geosciences*, 41, 927–945, <https://doi.org/10.1007/s11004-009-9244-2>, 2009.
- Caumon, G., Gray, G., Antoine, C., and Titeux, M.-O.: Three-dimensional implicit stratigraphic model building from remote sensing data on tetrahedral meshes: theory and application to a regional model of La Popa Basin, NE Mexico, *IEEE Transactions on Geoscience and Remote Sensing*, 51, 1613–1621, 2012.
595
- Chaodong, F., Peng, Y., and Bo, X.: Rapid geological modeling by using implicit 3D potential field interpolation method, in: *2010 International Conference On Computer Design and Applications*, vol. 5, pp. V5–50, IEEE, 2010.
- Chen, Y., Jiang, H., Li, C., Jia, X., and Ghamisi, P.: Deep feature extraction and classification of hyperspectral images based on convolutional neural networks, *IEEE Transactions on Geoscience and Remote Sensing*, 54, 6232–6251, 2016.
- 600 Chiles, J.-P., Aug, C., Guillen, A., and Lees, T.: Modelling the geometry of geological units and its uncertainty in 3D from structural data: the potential-field method, in: *Proceedings of international symposium on orebody modelling and strategic mine planning*, Perth, Australia, vol. 22, p. 24, Citeseer, 2004.
- Chollet, F.: Xception: Deep learning with depthwise separable convolutions, in: *Proceedings of the IEEE conference on computer vision and pattern recognition*, pp. 1251–1258, 2017.
- 605 Collon, P., Steckiewicz-Laurent, W., Pellerin, J., Laurent, G., Caumon, G., Reichart, G., and Vaute, L.: 3D geomodelling combining implicit surfaces and Voronoi-based remeshing: A case study in the Lorraine Coal Basin (France), *Computers & Geosciences*, 77, 29–43, 2015.
- Cook, R. L.: Stochastic sampling in computer graphics, *ACM Transactions on Graphics (TOG)*, 5, 51–72, 1986.
- de Kemp, E., Jessell, M., Aillères, L., Schetselaar, E., Hillier, M., Lindsay, M., and Brodaric, B.: Earth model construction in challenging geologic terrain: Designing workflows and algorithms that makes sense, in: *Proceedings of exploration*, vol. 17, pp. 419–439, 2017.
- 610 Donmez, P.: *Introduction to Machine Learning*, by Ethem Alpaydin, 2010.
- Fabin, C. E., Correia Filho, O. J., Alencar, M. L., Barbosa, J. A., MIRANDA, T. S., Neumann, V. H., Gomes, I. F., and SANTANA, F. R.: Stratigraphic relations of the Ipubi formation: siliciclastic-evaporitic succession of the Araripe Basin, *Anais da Academia Brasileira de Ciências*, 90, 2049–2071, 2018.
- Fornberg, B.: Generation of finite difference formulas on arbitrarily spaced grids, *Mathematics of computation*, 51, 699–706, 1988.
- 615 Fossen, H.: *Structural geology*, Cambridge University Press, 2016.
- Geng, Z., Wu, X., Shi, Y., and Fomel, S.: Deep learning for relative geologic time and seismic horizons, *Geophysics*, 85, WA87–WA100, 2020.

- Grose, L., Laurent, G., Aillères, L., Armit, R., Jessell, M., and Cousin-Dechenaud, T.: Inversion of Structural Geology Data for Fold Geometry, *Journal of Geophysical Research: Solid Earth*, 123, 6318–6333, <https://doi.org/10.1029/2017JB015177>, 2018.
- 620 Grose, L., Aillères, L., Laurent, G., Caumon, G., Jessell, M., and Armit, R.: Modelling of faults in LoopStructural 1.0, *Geoscientific Model Development*, 14, 6197–6213, <https://doi.org/10.5194/gmd-14-6197-2021>, 2021.
- Hennenfent, G. and Herrmann, F. J.: Simply denoise: Wavefield reconstruction via jittered undersampling, *Geophysics*, 73, V19–V28, 2008.
- Hillier, M., Wellmann, F., Brodaric, B., de Kemp, E., and Schetselaar, E.: Three-Dimensional Structural Geological Modeling Using Graph Neural Networks, *Mathematical Geosciences*, 53, 1725–1749, 2021.
- 625 Hillier, M. J., Schetselaar, E. M., de Kemp, E. A., and Perron, G.: Three-dimensional modelling of geological surfaces using generalized interpolation with radial basis functions, *Mathematical Geosciences*, 46, 931–953, 2014.
- Howard, A., Sandler, M., Chu, G., Chen, L.-C., Chen, B., Tan, M., Wang, W., Zhu, Y., Pang, R., Vasudevan, V., et al.: Searching for mobilenetv3, in: *Proceedings of the IEEE/CVF International Conference on Computer Vision*, pp. 1314–1324, 2019.
- Howard, A. G., Zhu, M., Chen, B., Kalenichenko, D., Wang, W., Weyand, T., Andreetto, M., and Adam, H.: Mobilenets: Efficient convolutional neural networks for mobile vision applications, *arXiv preprint arXiv:1704.04861*, 2017.
- 630 Hu, J., Shen, L., and Sun, G.: Squeeze-and-excitation networks, in: *Proceedings of the IEEE conference on computer vision and pattern recognition*, pp. 7132–7141, 2018.
- Iandola, F. N., Han, S., Moskewicz, M. W., Ashraf, K., Dally, W. J., and Keutzer, K.: SqueezeNet: AlexNet-level accuracy with 50x fewer parameters and < 0.5 MB model size, *arXiv preprint arXiv:1602.07360*, 2016.
- 635 Jessell, M.: Three-dimensional geological modelling of potential-field data, *Computers & Geosciences*, 27, 455–465, 2001.
- Jessell, M., Guo, J., Li, Y., Lindsay, M., Scalzo, R., Giraud, J., Pirot, G., Cripps, E., and Ogarko, V.: Into the Noddyverse: a massive data store of 3D geological models for machine learning and inversion applications, *Earth System Science Data*, 14, 381–392, 2022.
- Kingma, D. P. and Ba, J.: Adam: A method for stochastic optimization, *arXiv preprint arXiv:1412.6980*, 2014.
- Kirkwood, C., Economou, T., Pugeault, N., and Odbert, H.: Bayesian Deep Learning for Spatial Interpolation in the Presence of Auxiliary Information, *Mathematical Geosciences*, 54, 507–531, <https://doi.org/10.1007/s11004-021-09988-0>, 2022.
- 640 Lajaunie, C., Courrioux, G., and Manuel, L.: Foliation fields and 3D cartography in geology: principles of a method based on potential interpolation, *Mathematical Geology*, 29, 571–584, 1997.
- Laurent, G., Aillères, L., Caumon, G., and Grose, L.: Folding and poly-deformation modelling in implicit modelling approach, 34th Gocad Meet. Proc, pp. 1–18, 2014.
- 645 Li, Z., Pan, M., Han, D., Liu, W., Hu, S., Liu, P., and Yan, M.: Three-Dimensional Structural Modeling Technique, *Earth Science*, 41, 2136–2146, 2016.
- Lin, T.-Y., Dollár, P., Girshick, R., He, K., Hariharan, B., and Belongie, S.: Feature pyramid networks for object detection, in: *Proceedings of the IEEE conference on computer vision and pattern recognition*, pp. 2117–2125, 2017.
- Lindsay, M. D., Aillères, L., Jessell, M. W., de Kemp, E. A., and Betts, P. G.: Locating and quantifying geological uncertainty in three-dimensional models: Analysis of the Gippsland Basin, southeastern Australia, *Tectonophysics*, 546, 10–27, 2012.
- 650 Maggiori, E., Tarabalka, Y., Charpiat, G., and Alliez, P.: Convolutional neural networks for large-scale remote-sensing image classification, *IEEE Transactions on geoscience and remote sensing*, 55, 645–657, 2016.
- Mallet, J.: Three-dimensional graphic display of disconnected bodies, *Mathematical geology*, 20, 977–990, 1988.
- Mallet, J.-L.: Discrete smooth interpolation in geometric modelling, *Computer-aided design*, 24, 178–191, 1992.
- 655 Mallet, J.-L.: Discrete modeling for natural objects, *Mathematical geology*, 29, 199–219, 1997.

Mallet, J.-L.: Elements of mathematical sedimentary geology: The GeoChron model, EAGE publications, 2014.

McInerney, P., Goldberg, A., Calcagno, P., Courrioux, G., Guillen, A., and Seikel, R.: Improved 3D geology modelling using an implicit function interpolator and forward modelling of potential field data, in: Proceedings of exploration, vol. 7, pp. 919–922, 2007.

Perol, T., Gharbi, M., and Denolle, M.: Convolutional neural network for earthquake detection and location, Science Advances, 4, e1700578, 2018.

Phillips, J. D., Hansen, R. O., and Blakely, R. J.: The use of curvature in potential-field interpretation, Exploration Geophysics, 38, 111–119, 2007.

Pirot, G., Joshi, R., Giraud, J., Lindsay, M. D., and Jessell, M. W.: loopUI-0.1: uncertainty indicators to support needs and practices in 3D geological modelling uncertainty quantification, Geoscientific Model Development Discussions, pp. 1–31, 2022.

Renaudeau, J., Malvesin, E., Maerten, F., and Caumon, G.: Implicit structural modeling by minimization of the bending energy with moving least squares functions, Mathematical Geosciences, 51, 693–724, 2019.

Ronneberger, O., Fischer, P., and Brox, T.: U-net: Convolutional networks for biomedical image segmentation, in: International Conference on Medical image computing and computer-assisted intervention, pp. 234–241, Springer, 2015.

Sandler, M., Howard, A., Zhu, M., Zhmoginov, A., and Chen, L.-C.: Mobilenetv2: Inverted residuals and linear bottlenecks, in: Proceedings of the IEEE conference on computer vision and pattern recognition, pp. 4510–4520, 2018.

Shewchuk, J.: What is a good linear finite element? interpolation, conditioning, anisotropy, and quality measures (preprint), University of California at Berkeley, 73, 137, 2002.

Shi, Y., Wu, X., and Fomel, S.: SaltSeg: Automatic 3D salt segmentation using a deep convolutional neural network, Interpretation, 7, SE113–SE122, 2019.

Souche, L., Iskenova, G., Lepage, F., Desmarest, D., et al.: Construction of structurally and stratigraphically consistent structural models using the volume-based modelling technology: Applications to an Australian dataset, in: International petroleum technology conference, International Petroleum Technology Conference, 2014.

Viard, T., Caumon, G., and Levy, B.: Adjacent versus coincident representations of geospatial uncertainty: Which promote better decisions?, Computers & Geosciences, 37, 511–520, 2011.

Wang, Z., Simoncelli, E. P., and Bovik, A. C.: Multiscale structural similarity for image quality assessment, in: The Thirty-Seventh Asilomar Conference on Signals, Systems & Computers, 2003, vol. 2, pp. 1398–1402, Ieee, 2003.

Wang, Z., Bovik, A. C., Sheikh, H. R., and Simoncelli, E. P.: Image quality assessment: from error visibility to structural similarity, IEEE transactions on image processing, 13, 600–612, 2004.

Wellmann, F. and Caumon, G.: 3-D Structural geological models: Concepts, methods, and uncertainties, in: Advances in Geophysics, vol. 59, pp. 1–121, Elsevier, 2018.

Wu, X., Liang, L., Shi, Y., and Fomel, S.: FaultSeg3D: using synthetic datasets to train an end-to-end convolutional neural network for 3D seismic fault segmentation, GEOPHYSICS, 84, IM35–IM45, 2019.

Wu, X., Geng, Z., Shi, Y., Pham, N., Fomel, S., and Caumon, G.: Building realistic structure models to train convolutional neural networks for seismic structural interpretation, Geophysics, 85, WA27–WA39, 2020.

Wu, Y., Lin, Y., Zhou, Z., Bolton, D. C., Liu, J., and Johnson, P.: DeepDetect: A cascaded region-based densely connected network for seismic event detection, IEEE Transactions on Geoscience and Remote Sensing, 57, 62–75, 2018.

Yeh, R. A., Chen, C., Yian Lim, T., Schwing, A. G., Hasegawa-Johnson, M., and Do, M. N.: Semantic image inpainting with deep generative models, in: Proceedings of the IEEE conference on computer vision and pattern recognition, pp. 5485–5493, 2017.

- Yu, C., Wang, J., Peng, C., Gao, C., Yu, G., and Sang, N.: Learning a discriminative feature network for semantic segmentation, in: Proceedings of the IEEE conference on computer vision and pattern recognition, pp. 1857–1866, 2018a.
- Yu, J., Lin, Z., Yang, J., Shen, X., Lu, X., and Huang, T. S.: Generative image inpainting with contextual attention, in: Proceedings of the IEEE conference on computer vision and pattern recognition, pp. 5505–5514, 2018b.
- Zhao, H., Gallo, O., Frosio, I., and Kautz, J.: Loss functions for image restoration with neural networks, *IEEE Transactions on computational imaging*, 3, 47–57, 2016.
- 700 Zhou, Z., Siddiquee, M. M. R., Tajbakhsh, N., and Liang, J.: Unet++: A nested u-net architecture for medical image segmentation, in: Deep learning in medical image analysis and multimodal learning for clinical decision support, pp. 3–11, Springer, 2018.